

https://dspace.org/

Multi-Resolution Modelling of the Underground Mining Workplace by Integrating Laser Scanning and Close-Range Photogrammetry

Musiyiwa, Farai

2024

University of the Witwatersrand, Johannesburg

https://hdl.handle.net/10539/50111

Musiyiwa, Farai. (2024). Multi-Resolution Modelling of the Underground Mining Workplace by Integrating Laser Scanning and Close-Range Photogrammetry. [Master's dissertation, University of the Witwatersrand, Johannesburg]. WIReDSpace. https://hdl.handle.net/10539/50111

Downloaded from a DSpace repository. https://dspace.org/

School of Mining Engineering



UNIVERSITY OF THE
WITWATERSRAND,
JOHANNESBURG

MULTI-RESOLUTION MODELLING OF THE UNDERGROUND MINING WORKPLACE BY INTEGRATING LASER SCANNING AND CLOSE-RANGE PHOTOGRAMMETRY

Farai Musiyiwa

I declare that this research dissertation is my own unaided work. It is being submitted for the degree of Master of Science at the University of the Witwatersrand, Johannesburg. It has not been submitted before for any degree or examination to any other university.

Johannesburg, 2024

DECLARATION

I declare that this dissertation is my own unaided work. It is being submitted for the degree of Master of Science at the University of the Witwatersrand, Johannesburg. It has not been submitted before for any degree or examination to any other university. I have familiarised myself with the University of the Witwatersrand Student Academic Misconduct Policy (SAMP). I hereby declare that the work I am submitting for assessment is my original work. I affirm that I have not plagiarised, misrepresented, or colluded with any other person or source. I have properly acknowledged, cited, and referenced all the sources that I have used in my work. I also declare that I have used artificial intelligence (AI) tools only as a means of guidance. The ideas and arguments presented in my work are my original thoughts and interpretations. I acknowledge that any academic misconduct, such as plagiarism or collusion will result in serious consequences. These consequences may include a reduced grade, a fail mark, or disciplinary action according to the SAMP. The School of Mining Engineering has my consent to investigate any potential academic misconduct in my work. This investigation may include the use of similarity and AI detection software to check the originality of my work. I undertake to abide by the decision of any such investigation.



(Signature of Candidate)

01 day of October 2025

ABSTRACT

This research highlights the essential requirement for precise deformation monitoring in underground mining, where conventional measurement techniques frequently compromise mine personnel safety. The main aim of this research is to improve spatial accuracy in deformation monitoring by integrating terrestrial laser scanning (LiDAR) and close-range photogrammetry (CRP) datasets.

Data was acquired by both LiDAR and CRP technologies, and the data was integrated to produce a more accurate depiction of the underground mines. To assess the precision of the fused model, measurements derived from it were assessed using Mean Absolute Error (MAE), Root Mean Square Error (RMSE), and Mean Percentage Error as the principal evaluation metrics.

The fused 3D model displayed the lowest MAE and RMSE values relative to individual LiDAR and CRP data, indicating enhanced accuracy and diminished error margins. The integrated model attained a Mean Absolute Error (MAE) of 0.021 m (~2.1 cm) and a Root Mean Square Error (RMSE) of 0.027 m (~2.7 cm), demonstrating considerable accuracy compared to models from their respective sensors. In the context of underground deformation monitoring, where measurement tolerance of 5 cm or greater are often acceptable, these error magnitudes indicate high accuracy.

ACKNOWLEDGMENTS

The researcher would like to thank and acknowledge the financial support provided by Sibanye-Stillwater through the Sibanye-Stillwater Digital Mining Laboratory (DigiMine) at the Wits Mining Institute (WMI).

The researcher would like to thank his supervisors, Dr Muhammad Ahsan Mahboob and Dr Iqra Atif for their assistance throughout the course of this research. Not only did they provide more ideas on how to enhance the accuracy of the reconstructed 3D models, but also for the execution of the research in due time with better coherency and workflow of the research.

The researcher would like to also thank his retired supervisor, Mr Huw Thomas for his invaluable insights regarding this research. The research would not have been as concise, thorough and comprehensive without him.

The researcher extends gratitude to Maptek for supplying the terrestrial laser scanner equipment and the PointStudio software utilised for the 3D model reconstruction of LiDAR scans. Appreciation is also given to the Sibanye-Stillwater Digital Mining Laboratory (DigiMine) at the Wits Mining Institute (WMI) for facilitating access to these resources.

The researcher would also want to thank, last but not least, the Alpha and Omega, God for the guidance and making all this possible through His Grace!

Only forward!

TABLE OF CONTENTS

DECLARATION i

ABSTRACT ii

ACKNOWLEDGMENTS iii

LIST OF FIGURES viii

LIST OF TABLES xi

LIST OF EQUATIONS xii

LIST OF ABBREVIATIONS xiv

1 INTRODUCTION 1

1.1 Research Background and Context 1

1.1.1 Precautionary Measures 2

1.1.2 Causes and Impacts of FOGs 2

1.1.3 Traditional Methods for Discontinuities Geotechnical Data Collection 5

1.1.4 Introduction of Remote Sensing Technologies 6

1.1.5 Application of Light Detection and Ranging (LiDAR) for Data Collection 6

1.1.6 Use of Close-Range Photogrammetry (CRP) for Data Collection 11

1.2 Problem Statement 13

1.3 Research Objectives 14

1.4 Justification for Research 14

1.5 Structure of the Research Report 15

2 LITERATURE REVIEW 18

2.1 Introduction 18

2.2 Key Concepts, Theories and Studies 22

2.2.1 LiDAR Concepts 24
2.2.2 Photogrammetry Concepts 27
2.3 Key Debates and Controversies 31
2.4 Chapter Summary 37
3 RESEARCH METHODS 39
3.1 Steps Undertaken to Integrate LiDAR and CRP 39
3.2 Photogrammetry Components and their Parameters 43
3.2.1 DJI Osmo Stabilising gimbal 43
3.2.2 Android device 43
3.2.3 Photogrammetry Equations 45
3.3 LiDAR Components and their Parameters 48
3.3.1 Terrestrial Laser Scanner 48
3.3.2 Tripod 49
3.3.3 Hand-Held Controller (HHC) 50
3.3.4 LiDAR Equations 50
3.4 Wits Mock Mine 52
3.5 Research Design 54
3.6 Data Collection Process 56
3.8 Chapter Summary 58
4 DATA FOR THE STUDY 60
4.1 Point Cloud Density 60
4.2 Compatibility of Collected Data 64
4.3 Chapter Summary 66
5 RESULTS AND DISCUSSION 67
5.1 Introduction and Objectives of the Analysis 67
5.2 Data Acquisition and Registration of Point Clouds 68

5.2.1 Registration of LiDAR point clouds 68
5.2.2 Registration of CRP Point Clouds 72
5.3 Georeferencing in a Global Navigation Satellite System (GNSS)-Denied Underground Mine 75
5.3.1 Pre-Deformation and Post-Deformation Processing of LiDAR 3D Models 76
5.3.2 Pre- and Post-Deformation Processing of CRP 3D Models 78
5.4 Verification of Alignment 82
5.4.1 Alignment of Fused 3D Model Dense Point Clouds in the Pre-Deformation Stage 83
5.4.2 Alignment of Fused 3D Model Dense Point Clouds in the Post-Deformation Stage 84
5.5 Textured Mesh Generation of Combined Point Clouds 85
5.6 Accuracy Assessment 89
5.6.1 Mean Absolute Error 90
5.6.2 Root Mean Square Error (RMSE) 91
5.6.3 Percentage Error 93
5.6.4 Comparison and analysis of accuracy assessment metrics 94
5.7 Deformation Mapping and Monitoring 95
5.7.1 Point-to-Point Comparison 95
5.7.2 Heat Map 96
5.8 Chapter Summary 101
6 CONCLUSIONS, LIMITATIONS AND RECOMMENDATIONS 104
6.1 Conclusions 104
6.2 Recommendations 105
6.3 Limitation of Study and Future Research Work 106
7 REFERENCES 109

Appendix B LiDAR Data Acquisition in the Wits Mock Mine During the Post-Deformation Stage..... 121

Appendix C Registration of Pre-Deformation and Post-Deformation LiDAR Scans. 123

Appendix D Comparison of geometry and colour of objects from CRP, LiDAR and fused 3D model. 129

Appendix E Conventional Measurements of Objects using a Tape Measure ... 131

Appendix F Measurement of Objects using CRP. 133

Appendix G Measurement of Objects using LiDAR..... 135

Appendix H Measurement of Objects using Fused 3D Reconstructed Model... 137

LIST OF FIGURES

Figure 1.1: Stress transfer in a typical underground longwall mine. 3

Figure 1.2 Causes and indication of main dynamic disasters in deep mines . 5

Figure 1.3: Illustration of transmitted and reflected signals using the phase shift principle of a LiDAR. 8

Figure 1.4: Triangulation principle using LiDAR. 9

Figure 1.5: Illustration of time-of-flight principle using a laser scanner 11

Figure 2.1: Illustration of how changes in ISO, aperture and shutter speed affect the quality of images 30

Figure 3.1: Flowchart illustrating the fusion of LiDAR and CRP to reconstruct a photorealistic 3D model. 40

Figure 3.2: Principle of PDAF. 44

Figure 3.3: 3D model of a Wits mock mine used to illustrate the locations of the tunnel, stope panel and lamp room 54

Figure 3.4: Tape measure used for conventional measurements of varying components in the Wits mock mine tunnel including objects indicating post-deformation properties. 58

Figure 4.1: Indication of the number of points in the pre-deformation stage of a) decimated LiDAR point cloud model and b) CRP point cloud model. 62

Figure 4.2: Decimation of LiDAR point cloud in post-deformation to ensure there is consistency of point clouds between a) LiDAR and b) CRP point clouds. 63
Figure 5.1: Illustration of how LiDAR was positioned under each peg in the Wits mock mine. 69
Figure 5.2: Missing data observed in one of the LiDAR scans of Wits mock mine. 70
Figure 5.3: Illustration of (a) unregistered LiDAR scans and (b) registered LiDAR scans. 71
Figure 5.4: Registered point clouds in a reconstructed 3D model of the Wits mock mine tunnel using CRP principle. 75
Figure 5.5: Location of pegs in the Wits mock mine tunnel used to georeferenced LiDAR and CRP 3D models for this research. 76
Figure 5.6: Illustration of georeferenced LiDAR point clouds with GCPs correctly positioned. 78
Figure 5.7: Illustration of a peg detected on an image for georeferencing of CRP 3D models. 81
Figure 5.8: Georeferenced 3D model reconstructed using CRP principles, with GCPs incorporated within the model. 82
Figure 5.9: Fused 3D model from CRP and LiDAR point clouds in the pre-deformation stage. 83

Figure 5.10: Comparison of fused LiDAR and CRP point clouds with fluorescent tube objects in a) unstructured datasets and b) structured datasets. 84

Figure 5:11: Comparison of textural quality of Wits mock mine tunnel between a) a fused 3D reconstructed model and b) an image captured using an Android device. 86

Figure 5:12: ICP global residuals graph showing the accuracy of alignment of pre-deformation and post-deformation fused point clouds. 87

Figure 5.13: Comparison of the object dimensions obtained using a tape measure, CRP, LiDAR and fused 3D model. 90

Figure 5.14: Residual histogram indicating differences in points between pre-deformation and post-deformation. 95

Figure 5.15: A post-deformation 3D model heat map of the Wits mock mine tunnel. 97

Figure 5.16: A histogram illustrating the relationship between the number of points in the post-deformation 3D model with its residual……98

LIST OF TABLES

Table 2.1: Description of how most factors encountered in underground mines result in deformation 21

Table 2.2: Comparisons between LiDAR and digital camera sensors 33

Table 3.1: Main components used for data acquisition to reconstruct 3D models of Wits mock mine. 42

Table 3.2: Megapixels and apertures of the triple main camera sensors of Samsung A14 device. 44

Table 3.3: Objects positioned in Wits mock mine to depict post deformation conditions and the justifications for simulating these objects. 56

Table 5.1: Illustration of the code implemented in the SIFT feature detection algorithm. 73

Table 5.2: Pegs used to georeference a CRP reconstructed 3D model in the pre-deformation stage. 79

Table 5.3: Pegs used to georeference post-deformation 3D reconstructed model with their coordinates. 7978

Table 5.4: Summary of the calculated errors of CRP, LiDAR and fused 3D model metrics with observed measurements from the tape measure. 94

Table 5.5: Heat map of objects placed in the Wits mock mine tunnel representing deformation. 98

LIST OF EQUATIONS

Equation no. (1.1) 9

Equation no. (1.2) 10

Equation no. (2.1) 36

Equation no. (3.1) 45

Equation no. (3.2) 46

Equation no. (3.3) 46

Equation no. (3.4) 46

Equation no. (3.5) 46

Equation no. (3.6) 47

Equation no. (3.7) 47

Equation no. (3.8) 47

Equation no. (3.9) 47

Equation no. (3.10) 48

Equation no. (3.11) 48

Equation no. (3.12) 50

Equation no. (3.13) 51

Equation no. (3.14) 51

Equation no. (5.1) 91

Equation no. (5.2) 91

Equation no. (5.3) 91

Equation no. (5.4) 92

Equation no. (5.5) 92

Equation no. (5.6) 92

Equation no. (5.7) 93

Equation no. (5.8) 93

Equation no. (5.9) 93

LIST OF ABBREVIATIONS

AMCW	Amplitude-modulated continuous waves
BLE	Bluetooth Low Energy
CC	Cylindrical Container
CMCS	Camera coordinate system
CR	Concrete Rock
CRP	Close-range photogrammetry
CV	Computer Vision
DMRE	Department of Mineral Resources and Energy
FOG	Falls of Ground
FT	Fluorescent Tube
GCP	Ground control points
GDI	Gas detection instrumentation
GLCS	Global coordinate system
GNSS	Global Navigation Satellite System
ISO	International organisation for standardisation.
LiDAR	Light detection and ranging
MAE	Mean Absolute Error

MAPE	Mean absolute percentage error
MSE	Mean squared error
MVS	Multi-view stereo
NCSS	National Control Survey System
ORB	Oriented Fast and Rotated Brief
PC	Plastic Cup
PP	Plastic Plate
RANSAC	Random Sample Consensus
RFID	Radio-Frequency Identification
RMSE	Root Mean Square Error
SAR	Specific absorption rate
SfM	Structure from motion
SOCS	Laser scanner’s coordinate system
SP	Spherical Paper
SURF	Speeded-Up Robust Features
ToF	Time-of-flight
Wi-Fi	Wireless Fidelity
WSNs	Wireless sensor nod

1 INTRODUCTION

1.1 Research Background and Context

Mining is a key driver of economic growth, supplying vital raw materials for industries like construction, manufacturing, and energy. However, working underground comes with serious risks, particularly when it comes to ground stability. One of the biggest dangers is falls of ground (FOG), which threaten both worker safety and infrastructure integrity. Preventing these incidents requires a deep understanding of the geological factors at play, along with effective monitoring strategies. Technologies like terrestrial laser scanning (LiDAR) and close-range photogrammetry (CRP) have emerged as valuable tools for detecting and tracking ground movement in underground mines. By incorporating these methods, mining operations can improve their ability to assess risks, enhance safety measures, and boost overall efficiency.

Advanced scanning and imaging technologies have become essential for tracking structural changes in underground mines. These tools allow for continuous monitoring of rock behavior, offering valuable insights into how deformation develops over time. Early detection is crucial, as it enables mining teams to take proactive steps to reduce risks and safeguard both workers and infrastructure (Benton et al., 2016).

When deformation is identified, monitoring the rate of structural shifts becomes a priority. This process involves analysing changes in rock formations over time to spot signs of instability. By using a time-based

approach to assess rock movement, mining operations can better predict potential failures and take action before accidents or collapses occur, significantly improving safety underground.

1.1.1 Precautionary Measures

Implementing automated alert systems is a crucial strategy for improving safety in underground mining. These systems detect deformation patterns and provide real-time warnings, allowing for the timely evacuation of personnel before conditions become hazardous. Ground deformation is often an early indicator of instability, influenced by factors such as overburden pressure, mining-induced stress, fault zones, and geological discontinuities (Li et al., 2018). By systematically monitoring these changes, mining operations can identify structural weaknesses at an early stage, reducing the risk of falls of ground (FOG) incidents and strengthening overall workplace safety.

1.1.2 Causes and Impacts of FOGs

FOGs incidents commonly occur when the hanging wall or rock face becomes exposed after blasting or mechanical cutting. Relying solely on visual inspections is often inadequate for detecting subtle deformation, highlighting the need for advanced remote sensing technologies to monitor stress variations in underground rock masses. Both vertical and horizontal stress distributions play a critical role in determining rock stability and the likelihood of structural failure (Vorster & Franklin, 2008; Li et al., 2018).

Stress redistribution is particularly significant in longwall mining operations, as illustrated in Figure 1.1, where changes in stress patterns can greatly influence ground stability. The integration of terrestrial laser scanning and photogrammetry allows for precise deformation measurement, providing essential data for risk assessment, preventive measures, and improved mine design.

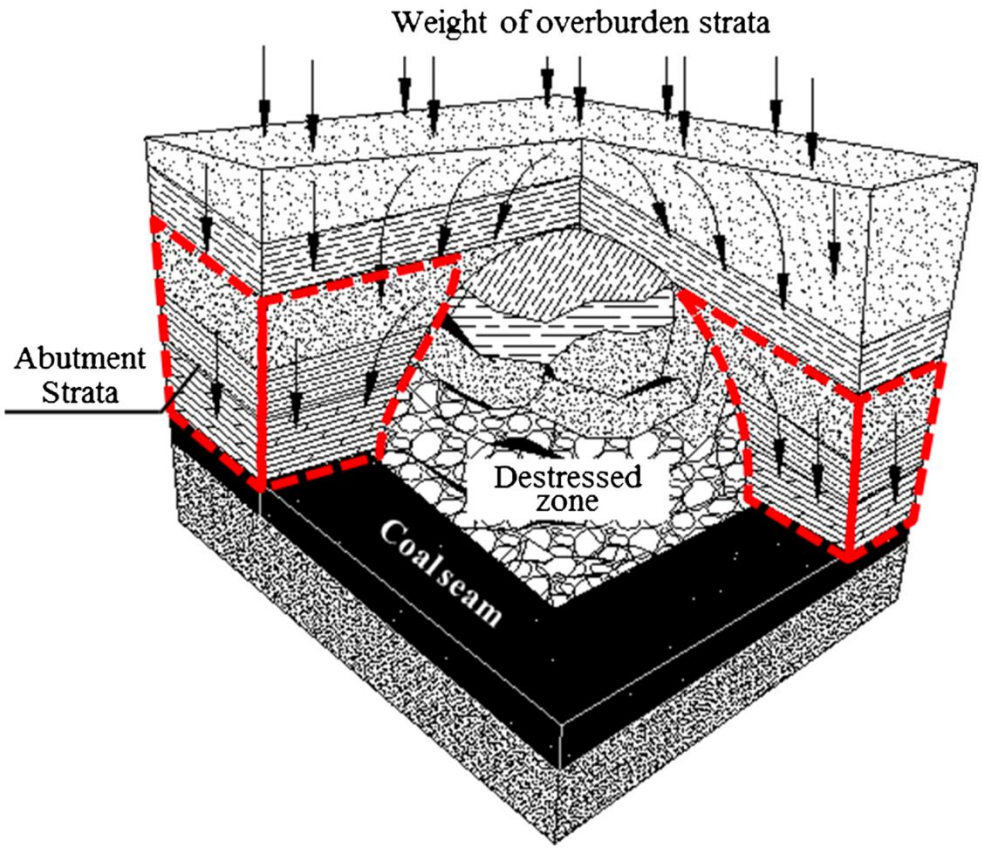


Figure 1.1: Stress transfer in a typical underground longwall mine (Li et al., 2018).

Underground mining environments pose significant hazards to mine personnel, primarily due to the instability of rock masses, which can lead to sudden collapses and entrapment. Such incidents not only threaten worker

safety but also increase the risk of severe injuries and fatalities. To mitigate these dangers, comprehensive inspections of underground workplaces are essential for identifying potential FOG and implementing proactive safety measures (Benton et al., 2016).

These inspections are conducted at critical stages, including before mining operations commence, following significant changes in ground conditions such as seismic events, and after each work shift. Various geological and environmental factors contribute to FOG incidents, including weak rock joints, mining-induced stresses, and adverse underground conditions such as extreme temperatures and high humidity levels (Slaker, 2015; He & Wang, 2023).

Figure 1.2 illustrates the key factors that contribute to underground mining disasters, including sudden, high-intensity rock failures. This research focuses on monitoring unpredictable solid dynamic disasters, as depicted in Figure 1.2. A detailed examination of these factors, their impact on rock stability, and relevant findings from previous studies is provided in the Literature Review chapter.

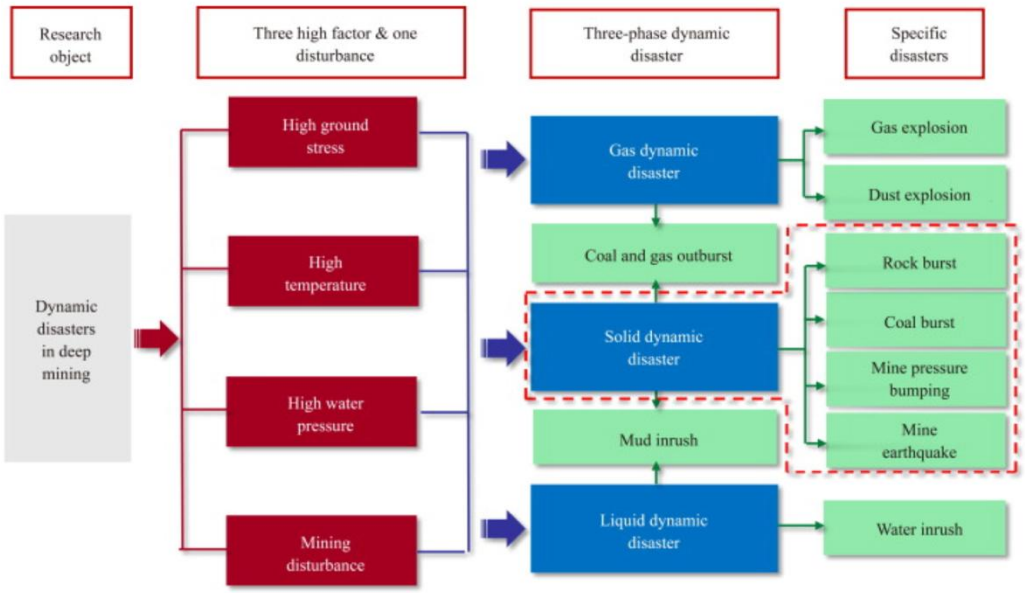


Figure 1.2 Causes and indication of main dynamic disasters in deep mines (He & Wang, 2023).

1.1.3 Traditional Methods for Discontinuities Geotechnical Data Collection

Traditionally, geotechnical data collection in underground mining has relied on instruments such as inclinometers, tape measures, extensometers, and compasses (Lato & Voge, 2012). While these tools provide direct measurements and structural evaluations, their use often necessitates personnel working in hazardous environments, increasing the risk of injury or fatality from FOG during data acquisition.

A further drawback of conventional methods is their inefficiency in data collection. Since the late 1990s and early 2000s, the adoption of remote sensing technologies has grown among geotechnical engineers, primarily due to their capacity to acquire large volumes of spatially accurate data in a

shorter time frame (Lato & Voge, 2012). The need for precise deformation monitoring has further accelerated the use of these advanced techniques, which have gained increasing prominence in geotechnical engineering since 2012 (Slaker, 2015).

1.1.4 Introduction of Remote Sensing Technologies

Over time, remote sensing technologies have undergone significant advancements, particularly in areas such as data fusion, deep learning applications, object detection and machine learning integration (Ma et al., 2019). As a non-contact method of data acquisition, remote sensing facilitates geotechnical assessments without physically altering the surveyed environment (Elachi & Zyl, 2021).

A range of sensors is utilised in remote sensing, each designed for specific applications, including data collection, surveying and environmental monitoring, all while preserving the natural state of the rock mass (Slaker, 2015). This study explores the application of remote sensing technologies in enhancing safety within underground mining operations, with a focus on detecting rock mass movements. By enabling continuous, non-intrusive data acquisition, remote sensing offers a reliable approach for monitoring ground deformation and reducing geotechnical hazards.

1.1.5 Application of Light Detection and Ranging (LiDAR) for Data Collection

Light Detection and Ranging (LiDAR) technology enables the rapid acquisition of high-density point cloud data, capturing millions of data points

per second with exceptional accuracy (Bhatti et al., 2021). This process is carried out using a laser scanner that functions based on LiDAR principles (Altuntas, 2021). In this study, the term "LiDAR" will be used to encompass laser scanning techniques. The efficiency of data collection is influenced by the scanner's technical specifications and configuration settings, with strategic placement being essential for achieving comprehensive coverage in underground mining environments.

LiDAR systems operate based on three primary principles: phase shift, triangulation, and ToF (Berberan et al., 2007). While each method is capable of generating precise and dense point cloud data, they vary in their respective advantages and limitations.

a) Phase Shift Principle

The phase shift principle is commonly employed for short-range data collection, providing greater ranging accuracy than the ToF method (Berberan et al., 2007). As depicted in Figure 1.3, this technique operates by emitting amplitude-modulated continuous waves (AMCW) and determining the distance to the target based on the phase difference between the transmitted and reflected signals (Wang et al., 2020).

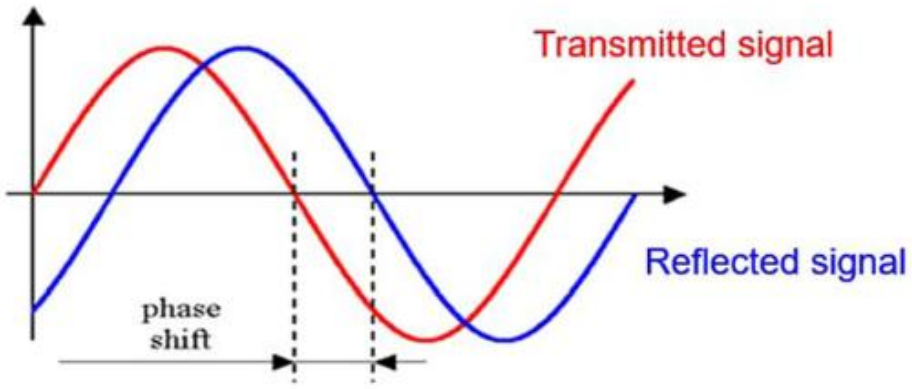


Figure 1.3: Illustration of transmitted and reflected signals using the phase shift principle of a LiDAR (Wang et al., 2020).

b) Triangulation Principle

Triangulation is a key measurement technique in remote sensing, used to accurately determine the location of surveyed environments by referencing pre-established coordinate points (Altuntas, 2021). This method is integral to LiDAR-based measurements, enabling precise spatial positioning of objects within the scanned area.

As shown in Figure 1.4, the triangulation principle relies on a known baseline distance and two measured angles—alpha (α) and beta (β)—to compute the remaining dimensions of the triangle formed between the LiDAR system and the target object. Once these angles are established, the exact position of the surveyed object is calculated using trigonometric relationships.

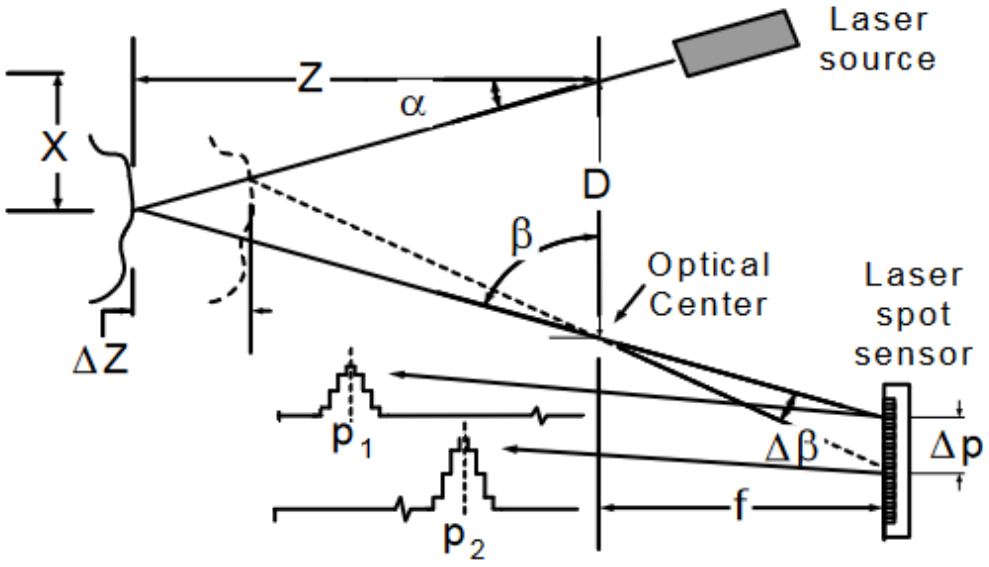


Figure 1.4: Triangulation principle using LiDAR (Beraldin, 2004).

The accuracy of triangulation-based measurements is influenced by factors such as the target's distance and the baseline separation between the camera and reference points. Equation (1.1) mathematically represents this relationship, illustrating how uncertainties in depth (Z) are affected by variations in the system's baseline and target distance (Beraldin, 2004). This technique is particularly effective for close-range LiDAR applications, where high-precision mapping of small-scale features is essential.

$$\sigma_z \approx \frac{Z^2}{fD}\sigma_p \tag{0.1}$$

Where: f is effective position of the laser spot sensor, D is the camera baseline, σ_p is uncertainty in the laser spot position and Z is the distance to the object. Different parameters determine the speckle noise on the spot position. The speckle noise is derived as shown in equation (1.2).

$$\sigma_p \approx \frac{1}{\sqrt{2\pi}} \lambda \, fn \quad (0.2)$$

Where: fn is the receiving lens f-number and λ is the laser wavelength.

c) Time-of-flight Principle

The ToF principle is the fundamental ranging method used by many LiDAR systems to determine the distance between the sensor and a target surface. In this approach, the LiDAR instrument emits a short pulse of laser light towards the object. The pulse travels through the medium, reflects off the target, and returns to the receiver within the LiDAR sensor as shown in Figure 1.5.

The process is repeated for many pulses per second while the LiDAR unit scans its environment, producing a dense collection of distance measurements that are converted into a three-dimensional point cloud. The accuracy of ToF LiDAR depends on the precision of its timing electronics, the reflectivity of the target surface, atmospheric conditions, and the beam divergence. In underground mining applications, where dust, humidity, and irregular surfaces are common, these factors must be considered to ensure reliable distance measurements.



Figure 1.5: Illustration of time-of-flight principle using a laser scanner (Kaldén & Sternå, 2015).

1.1.6 Use of Close-Range Photogrammetry (CRP) for Data Collection

Close-range photogrammetry (CRP) is a remote sensing technique used to extract accurate spatial information about physical objects and their surrounding environment through the capture, recording, and interpretation of overlapping photographic images (Wang et al., 2020). Advanced methodologies have been developed to generate three-dimensional (3D) models from these images, with Structure from Motion (SfM) and Multi-View Stereo (MVS) among the most widely adopted techniques (Wang et al., 2020).

Both SfM and MVS rely on core photogrammetric principles, enabling the reconstruction of 3D models using cost-effective digital cameras. The SfM process requires each image to contain at least three corresponding angles derived from convergent viewpoints, allowing for precise feature matching and model generation (Costantino et al., 2020).

Factors Influencing 3D Model Reconstruction in Photogrammetry include:

- Image Quality: the resolution of captured images plays a critical role in determining the accuracy of reconstructed 3D models. High-resolution images, typically those with a resolution of six megapixels or higher, significantly enhance the precision of model reconstruction (Beraldin et al., 2004). Even low-cost camera sensors can generate detailed and accurate 3D models when image quality is sufficiently high.
- Image Overlap: the degree of overlap between images is a key factor in photogrammetric reconstruction. Greater image overlap improves the ability of the SfM algorithm to detect feature correspondences, leading to more accurate reconstructions of complex underground environments. Additionally, the dense point clouds produced through SfM can be further refined using the MVS algorithm, which enhances resolution and surface detail (Costantino et al., 2020).
- Precision of Point Clouds: the accuracy of the generated point cloud is influenced by the pixel size of the captured area, as well as the quality and configuration of the camera system (Grussenmeyer et al., 2012). In photogrammetry, point clouds represent three-dimensional spatial coordinates (x, y, z), corresponding to horizontal positioning, vertical positioning, and depth relative to a reference point. A higher density of point clouds results in improved spatial resolution, which is particularly beneficial for monitoring and analysing underground mining environments.

1.2 Problem Statement

Reconstructing a high-precision and reliable 3D model of an underground mining environment presents considerable challenges due to the complex and dynamic nature of these settings. A range of environmental and operational factors must be carefully assessed to ensure that the generated models effectively capture rock mass deformation and support geotechnical stability evaluations. This study investigates the integration of Close-Range Photogrammetry (CRP) and Light Detection and Ranging (LiDAR) as a complementary approach to addressing the limitations of standalone remote sensing techniques.

Factors such as poor lighting, dust, humidity and smoke can degrade the quality of data collected by remote sensing systems, resulting in inconsistencies in the reconstructed 3D models (Slaker, 2015). Additionally, prolonged exposure to these conditions may accelerate the degradation of camera and LiDAR sensors, further affecting data reliability (Papachristos et al., 2019). One of the primary challenges in underground photogrammetry is the variability in lighting conditions, which can diminish image clarity and hinder feature detection.

By integrating CRP and LiDAR point clouds, this study aims to develop detailed and accurate spatial representations of underground mining environments. These models serve as essential tools for resource management, safety assessments, and operational optimization, ultimately

enhancing efficiency in mapping, deformation monitoring, and geotechnical risk management.

1.3 Research Objectives

The success of this research will be determined by achieving greater spatial precision in reconstructing the 3D model, thereby addressing safety issues prevalent in underground mining workplaces.

The following are the research objectives:

1. Collection of data using a terrestrial laser scanner and close-range photogrammetry;

2. Reconstructing 3D models using terrestrial laser scanner and photogrammetry datasets for deformation mapping and monitoring; and

3. Accuracy assessment using statistical parameters approach which includes root mean square error (RMSE), mean absolute error (MAE) and percentage of error.

1.4 Justification for Research

Safety is a critical concern in underground mining due to the high-risk conditions inherent to these environments. Proximity to geotechnical hazards, including areas prone to instability, often necessitates restricted

access to protect personnel. These risks underscore the importance of minimizing direct human exposure to hazardous zones. Remote sensing technologies offer a practical solution by enabling non-contact data acquisition, thereby reducing the need for workers to enter dangerous areas.

The effectiveness of remote sensing in improving safety, however, depends largely on how well these technologies are tailored to the specific needs and operational objectives of the mining site. Proper configuration and deployment are essential to ensure accurate monitoring of ground conditions, effective hazard identification, and risk mitigation. When implemented correctly, these technologies contribute significantly to enhancing both safety and operational efficiency within the underground mining sector.

1.5 Structure of the Research Report

This research report consists of six chapters. Chapter 1 is the introduction which covers the background of the research topic, problem statement, justification for the research, and research objectives. The background of the research topic first explains traditional methods and ways used before the implementation of CRP and LiDAR in underground mines. This section explains why CRP and LiDAR were introduced and how they are implemented in underground mines for safety purposes. The problem statement section explains how the fusion of CRP and LiDAR enhances

safety compared to the already existing methods for deformation mapping and monitoring.

Chapter 2 explains the literature review of this research. This includes key concepts theories, and studies from different sources related to the use of remote sensing technologies to improve safety in underground mines and achieve an almost zero-harm workplace. Key debates and controversies from various sources related to this study will also be highlighted in this chapter. These points will form the basis of this report.

Chapter 3 explains the research approach used from the preparation of data collection to the accuracy assessment of the 3D models reconstructed. A thorough assessment of the sources of data, area of research, and equipment used for data acquisition is put into account in this chapter. This research approach is explained in Chapter 3. Some limitations are reviewed, and reasons are further elaborated on why the particular research approach was used.

Chapter 4 investigates the data used for the study. This chapter explains further why collected datasets are relevant for this study. The relevance of the data collected is based on the hotspot area where deformation mapping and monitoring will be assessed.

Chapter 5 is based more on the analysis of data collected and how it aligns with the research's objectives. This chapter also focuses on cleaning data to ensure only relevant data for this research is available. Two main sectors

which include 3D models discretely reconstructed by LiDAR and CRP are analysed before fusing the datasets to reconstruct a third 3D model. The chapter discusses how the accuracy of data collected in underground mines can later be implemented for the safety of mine personnel. This includes both the qualitative and quantitative research approaches.

Chapter 6 concludes the research and provides recommendations regarding challenges faced during the research. Recommendations are based on improvements that can be undertaken for the accuracy of the 3D models. Observations are also discussed in this chapter to provide clarity on why the approaches used in this research were chosen.

The chapter also explains limitations that were faced from data capturing to the reconstruction of 3D models. Lastly, the chapter will provide recommendations for future work. This section focuses more on what can potentially be done to improve the safety of mine personnel by implementing remote sensing technologies.

2 LITERATURE REVIEW

2.1 Introduction

Historically, FOG has been one of the most significant risks in underground mining, contributing to high rates of occupational injuries and fatalities. In 2008, FOG were identified as a leading cause of occupational injuries and fatalities in underground mines (Vorster & Franklin, 2008). However, recent statistics from the Department of Mineral Resources and Energy (DMRE) indicate a significant decline in FOG-related incidents in South African mines (DMRE, 2022). Between 2021 and 2022, fatalities resulting from FOG incidents dropped from 20 to 6, while FOG-related injuries decreased by 4% over the same period (DMRE, 2022). These figures reflect notable progress in underground mining safety, suggesting that improvements in monitoring techniques and the implementation of stricter safety protocols have played a key role in reducing FOG risks.

One of the significant reasons for mapping geological features is to anticipate probable rock mass instability (Basahel & Mitri, 2017). This can be done to determine the level of caution required to monitor the potential hazards in the underground mining workplace. Various geological factors must be considered before assessing any deformations occurring in the underground mining workplace (Basahel & Mitri. 2017). Some of these parameters include the orientation of the rock structure, block sizes and roughness of the rock which will be used to determine the type of support compatible with rocks underground (Lato & Voge, 2012).

Improving safety in underground mines can be achieved by mitigating risks that pose threats to mine personnel (Slaker, 2015). These risks can result in occupational fatalities, injuries and diseases which should be alleviated to achieve a zero-harm underground mine (Sadeghi et al., 2022). Contact and non-contact technologies can be implemented in underground mines to enhance safety and productivity (Slaker, 2015). This can be achieved by collecting relevant, accurate data that can be used for analysis before executing precautionary measures.

Both LiDAR and CRP technologies are increasingly being employed to bring awareness and monitor hazards that occur in underground mines (Wu & Tang, 2015). They can be considered complementary and not mutually independent of each other. This section will review how CRP and LiDAR principles were implemented in different studies to reconstruct a comprehensive 3D model. This section compares the implementation of contact and non-contact technologies in underground mines and analyses why non-contact technologies should be deployed compared to contact technologies. Furthermore, it highlights the necessity of employing both CRP and LiDAR technology in underground mines and the significance of integrating these two technologies.

Instruments used in contact technologies are in direct contact with the region where measurements are obtained. Some of these conventional instruments include an inclinometer, vibrating wire extensometer, crack meter and the installation of sensors (Jiang et al., 2022; Benton et al.,

2016)). The underground mining workplaces from which the conventional method is implemented are limited because the area is constrained (Benton et al., 2016). Another limitation includes the quantity of contact instruments used which can be labour-intensive and tedious to monitor (Ding et al., 2022).

Deploying contact technologies to potentially hazardous hotspots in underground mines guarantees to a certain extent that the risks have been identified and addressed. Due to the distinct responses of rock masses in underground mines during mining operations, it is necessary to employ various mitigation measures to reduce risks. Consequently, the capability of conventional instrumentation to efficiently monitor underground mines is restricted (Ding et al., 2022). It is labour-intensive to deploy contact technologies to all potentially hazardous hotspots due to the uncertainty of the rock mass responses.

The detection of most hotspots in underground mines that lead to unforeseen FOGs requires comprehensive monitoring of the whole underground mine (Benton et al., 2016). Several factors contribute to the deformation of rock masses, resulting in unforeseen development of FOG. Varying rock mass responses are influenced by different factors which are further explained in Table 2.1.

Table 2.1: Factors Contributing to Deformation in Underground Mines

Factors	Description	Sources
In-situ stress	The strength of different rock masses is affected by the geological conditions and depth of the mine.	Benton et al., 2016; Wang et al., 2020
Underground mine depth	Overburden results in stress and rock bursts. The deeper the mine, the more stress induced on rock masses surrounding the underground mining area.	He & Wang, 2023
Time-dependent activities	Stress in rocks proportionally increases with time.	Benton et al., 2016
Mining method	Underground mines which are located below open pits tend to have less stable rock masses. One of the reasons is the impact of open pit slopes on damage patterns.	Zhang et al., 2022
Water inflow	Water softens rock masses because of its ability to decrease strength of different rock types such as shale.	Sasaoka et al., 2016
Rock mass quality	This refers to the different rock mass properties and is one of the main two factors that affect rock mass stability, besides in-situ stress.	Wang et al., 2020
Support system	They can assist the rock masses from any rock failure due to deformations occurring in the underground mines.	Chikande & Zvarivadza, 2016

Temperature fluctuations	Numerical simulations were conducted in one of the studies to determine the effect of temperature fluctuations. It was concluded there is a high chance of cracks in rock masses occurring due to increase in tensile stress of heat transfer.	Wu et al., 2021; He and Wang, 2023.
Blasting and vibrations	Blasting results in severe vibrations which affect stability of rock masses. The severity of the rock blasts usually significantly affects the upper level compared to below the fault surface.	Bazzi et al., 2020

Remote sensing technologies encompass a wide range of space in underground mines allowing data acquisition from a safe and secure distance thus avoiding exposure to dangerous conditions (Benton et al., 2016). Hence, remote sensing technologies are crucial to achieving a nearly risk-free underground mining workplace compared to contact technologies (Ding et al., 2022).

2.2 Key Concepts, Theories and Studies

Remote sensing technologies can effectively reduce risks associated with underground mines by providing valuable information without requiring direct human involvement (Benton et al., 2016). It is necessary to be aware of several underground mining issues that limit data acquisition and deployment of CRP and LiDAR equipment (Singh et al., 2023). The

underground mining workplace is barely a testing facility for the most state-of-the-art technologies due to various common and atypical limitations encountered underground.

Most remote sensing technologies require a global positioning system (GPS) to achieve their maximum capabilities and map reconstructed 3D models to the real-world coordinate system (Papachristos et al., 2019). There is no GPS underground because satellite signals cannot penetrate underground (Seguel et al., 2022). As a result, other means of aligning reconstructed 3D models to the real-world coordinate system include pegs and survey points with known world coordinates.

Remote sensing technologies, such as LiDAR and CRP, are subject to laws in most underground mines (Slaker & Mohamed, 2017). The reasons for this include:

- safety concerns;
- need for privacy in the underground mining industry;
- requirement for operational confidentiality; and
- security risks.

Consequently, if a viable plan has been prepared for implementation in the underground workplace, remote sensing technologies are then deployed for data collection. Key issues to consider include data-collecting procedures and methodologies to ensure the accuracy and reliability of remote sensing technologies (Berberan et al., 2007). This guarantees the acquisition of a

sufficient amount of high-quality data, irrespective of the constraints imposed by the underground workplace. This also reduces downtime as data is only gathered in specific areas of interest (Berberan et al., 2007).

2.2.1 LiDAR Concepts

Although numerous articles have been published on LiDAR, most do not specifically focus on its application in underground mining environments. (Singh et al., 2023). Between 2010 and 2019, the use and study of LiDAR technology in underground mining experienced significant growth (Singh et al, 2023). Research during this time was primarily concentrated in Australia, the United States, Canada, and China, countries that lead in resource extraction and underground mining of metals and coal (Singh et al., 2023). However, research output saw a notable decline in 2019 due to the disruptions brought about by the COVID-19 pandemic (Singh et al., 2023). Despite this setback, the advancements achieved during the decade highlight the growing role of LiDAR in improving safety and operational efficiency in underground mining environments

In 2007, minimal research focused on using LiDAR for deformation monitoring (Pfeifer et al., 2007). LiDAR was mainly used to obtain geometric measurements in cultural heritage documentation and open-pit mining (Pfeifer et al., 2007). LiDAR can capture a complete dataset in the form of a dense 3D point cloud made up of millions of data points by scanning any structure in its area of vision (Wu & Tang, 2015). Implementation of LiDAR

improves mine safety as it is utilised to assess and monitor the stability of rock faces and slopes (Kolapo, 2019).

LiDAR can improve mine safety by monitoring high accuracy movement measurements, typically within a few millimetres. This level of accuracy allows LiDAR to detect over time even small movements that could indicate instability, enabling mine operators to mitigate risks before any significant incidents occur (Van der Merwe & Andersen, 2013).

Different precursory indicators such as pre-failure deformation, crack openings and micro-seismicity are detected over time by LiDAR in an underground mining environment. These indicators result in mitigation measures being implemented to reduce risks (Abellan et al., 2010). The rock mass movement that might have occurred due to instability can vary depending on the mine conditions because LiDAR can detect changes that may indicate instability (Singh et al., 2023).

The orientation of rock mass and any temporal changes in positions of the rock mass can be detected by LiDAR. It is important to be aware of and address the limitations of LiDAR to maximise the likelihood of accurate and dependable results.

Various factors hinder accurate measurements when using LiDAR in underground environment. Internal and external factors, primarily instrument imperfection and the surrounding environment from which data is collected have certain restrictions that should be assessed (Singh et al.,

2023). Analysing these factors provides the best approach to obtaining good data using LiDAR. Major problems encountered when implementing LiDAR for underground analysis are related to laborious instrumental setup, transporting the equipment underground, no visible line-of-sight and requiring a lot of processing power for scan co-registration.

Sensor beam divergence affects the accuracy of the laser in reaching its target as the distance increases (Singh et al., 2023). The accuracy of the LiDAR decreases as the distance between the target and the LiDAR source increases, due to the increased dispersion of photons from the LiDAR source. The target typically has identifiable features such as its reflectivity and scattering abilities that impact the intensity of the laser (Pfeifer et al., 2007). Accuracy assessment procedures can improve the quality of reconstructed 3D models by correcting identified errors in remote sensing equipment.

LiDAR plays a crucial role in improving safety monitoring within underground mining operations. Its applications extend across various areas, including mine ventilation, excavation planning, rescue operations, layout optimization, logistics management, and hazard identification both prior to and following the use of explosives (Singh et al., 2023). Owing to its versatility, LiDAR has the potential to become a transformative remote sensing technology for diverse mining activities.

Beyond safety monitoring, LiDAR is utilized to measure rib displacement, characterize rock mass properties, assess surface roughness, evaluate underbreak and overbreak, and automate the generation of mining maps (Slaker, 2015). One of its primary advantages is the ability to capture accurate data under difficult underground conditions, such as variable lighting, which can significantly impair the performance of Close-Range Photogrammetry (CRP). This resilience to environmental challenges makes LiDAR an indispensable tool, enhancing both precision and operational efficiency in underground mining by supporting data-driven decision-making.

2.2.2 Photogrammetry Concepts

Slaker & Mohamed (2017) identified image overlap as a key factor influencing the accuracy of 3D reconstructions in photogrammetry. Achieving reliable geometric accuracy and photorealistic analysis requires a minimum image overlap of 60%. Additionally, internal camera exposure settings play a critical role in determining the quality of reconstructed 3D models, particularly in the low-light conditions found in underground mining environments.

The exposure triangle refers to the interdependent relationship between shutter speed, focal ratio (aperture), and ISO speed three parameters that control the amount of light reaching the camera sensor. These settings directly affect image brightness, sharpness, and overall quality, all of which

are crucial for accurate photogrammetric data acquisition (Slaker & Mohamed, 2017; Santise et al., 2018).

1. Shutter Speed

Shutter speed determines how long the camera’s shutter remains open, allowing light to reach the sensor. Faster shutter speeds reduce exposure time and minimize motion blur, which is especially important when capturing handheld images. For photogrammetric purposes, a shutter speed faster than 1/60s is recommended when using a 35 mm lens to ensure sharp, high-quality images suitable for 3D model generation (Slaker & Mohamed, 2017).

2. Focal Ratio (Aperture)

The focal ratio, commonly referred to as the f-stop, controls the size of the camera's aperture, regulating the amount of light entering the lens. This value is inversely proportional to the aperture size; a lower f-stop value allows more light to enter, while a higher value reduces it. In underground environments, setting the focal ratio to the highest feasible value helps optimize the depth of field, enabling the capture of detailed structural features such as rock cleats (Slaker & Mohamed, 2017). Adjusting the aperture appropriately can also reduce root mean square (RMS) errors, thereby improving the accuracy and reliability of 3D model reconstructions.

3. ISO Speed

ISO speed controls the camera sensor's sensitivity to light, influencing the brightness of the captured image. In low-light conditions, such as those encountered in underground mines, increasing the ISO can improve image brightness, facilitating better data acquisition (Santise et al., 2018). However, higher ISO values introduce noise or graininess, which can degrade image quality. To minimize this issue, ISO settings should ideally remain between 100 and 400 (Slaker & Mohamed, 2017). Maintaining a low ISO, where possible, enhances image clarity and supports more accurate 3D reconstructions by reducing noise.

Figure 2.1 provides a visual overview of how variations in the exposure triangle parameters affect image quality, emphasising the balance between brightness, sharpness, and noise. This illustration highlights how optimal exposure settings can significantly enhance the accuracy of photogrammetric models, particularly for underground mining applications.

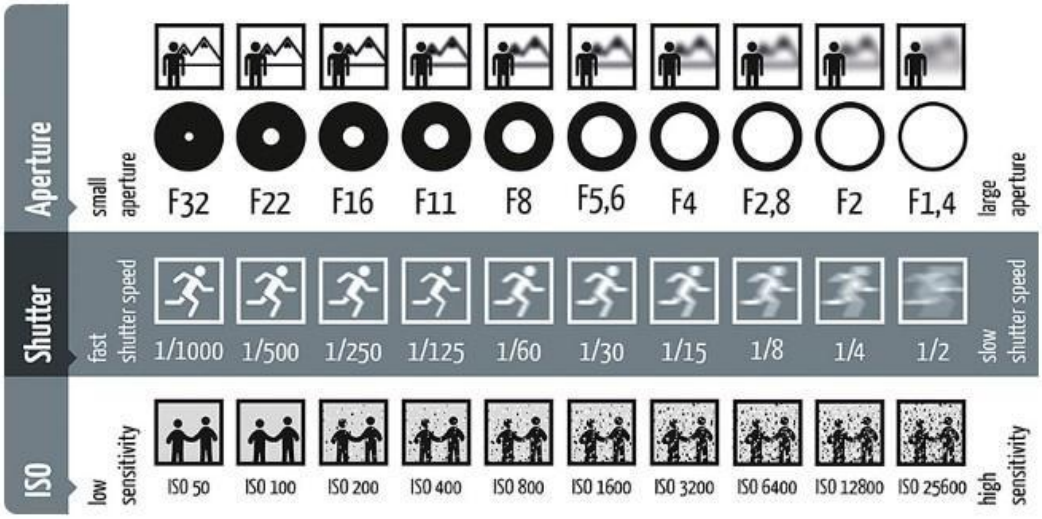


Figure 2.1: Illustration of how changes in ISO, aperture and shutter speed affect the quality of images (Hanssie, 2024).

Remote sensors can be utilised in underground mines to perform several functions, such as monitoring the deformation and movement of rock masses in underground mines. In the 1980s, CRP was already considered one of the most improved remote sensing technologies (Fraser & Brown, 1986). CRP enhances safety in underground mines because of its diverse usage.

Remote visual inspection can significantly reduce the time needed to go to the underground mine site. Captured images can serve several future objectives, such as assessing the quantity and quality of safety tools such as roof bolts and determining the types of rocks found underground. Benton and others (2016) state that CRP can also have a millimetre accuracy level.

2.3 Key Debates and Controversies

One major challenge in 3D model reconstruction is the exclusion of images with poor quality or insufficient overlap, which can significantly compromise the accuracy of photogrammetry. In underground mines, photogrammetry faces additional obstacles due to environmental factors such as fog, low lighting, dust, and complex geometries (Slaker, 2015). These adverse conditions impair sensor performance, requiring targeted measures to enhance data acquisition accuracy. Various studies have evaluated the feasibility of Close-Range Photogrammetry (CRP) for deformation monitoring, often achieving millimetre-level precision to meet deformation-related safety requirements (Benton et al., 2016).

Research in underground limestone mines highlights the benefits of combining LiDAR and CRP for rock mass deformation monitoring (Slaker, 2015). By collecting data at regular intervals, positional and volumetric changes in rock masses can be tracked, which enhances mine planning and supports the implementation of appropriate geotechnical support systems. This improved understanding of rock mass behavior not only boosts productivity but also enhances workplace safety by reducing geotechnical risks (Slaker, 2015).

Despite the advantages of combining LiDAR and CRP, certain limitations hinder the detailed reconstruction of 3D models. Forkuo (2005) identifies challenges related to generating accurate point clouds in underground environments, such as inconsistent data capture due to lighting and

structural complexity. His research highlights strategies to mitigate these challenges, including adjustments to data acquisition protocols and hybrid processing methods. Similarly, Singh et al. (2023) emphasize difficulties in obtaining comprehensive 3D models because of inaccuracies in underground point cloud data acquisition.

The potential of combining LiDAR and CRP technologies has also been demonstrated in other challenging environments, such as archaeological sites and landslide monitoring. Lerma et al. (2010) assessed model reliability in archaeological applications by evaluating graphic and metric factors, underscoring the importance of accurate data collection and processing methods. For landslide monitoring, Jiang et al., (2022) proposed strategies for acquiring data in difficult terrain with limited accessibility, achieving precise deformation measurements despite environmental constraints.

Forkuo (2005) further emphasizes the value of combining LiDAR and high-resolution CRP datasets, describing how hybrid matching techniques can improve model accuracy. His research presents detailed solutions for addressing data fusion challenges, enhancing the precision and reliability of reconstructed 3D models.

Technological advancements in both CRP and LiDAR have expanded their application in underground mining; however, each technology has distinct limitations. Table 2.2 compares the capabilities of CRP and LiDAR sensors,

highlighting their respective advantages, challenges, and data processing requirements. Addressing these limitations is essential to fully harness the benefits of CRP and LiDAR integration for underground mining operations.

Table 2.2: Comparisons between LiDAR and digital camera sensors

	LiDAR	**Digital Camera**	**Sources**
Spatial Resolution	High pixel intensity	Very high pixel intensity	Shan & Toth, 2018; Westoby et al., 2012
Texture Reconstructed	Low (lacks sufficient texture)	High (has sufficient texture or visual detail)	Micheletti et al., 2015; Westoby et al., 2012
Spatial Coverage	High	Medium	Shan & Toth, 2018; Westoby et al., 2012
Depth Accuracy	High (good precision when measuring surfaces)	High (good precision when measuring surfaces)	Jiang et al., 2022
Intensity/Colour	Low (limited ability to capture colour information)	High (has the capability of capturing good colour information)	ASPRS, 2019
Acquisition Procedure	Dynamic or static	Moment Shot	Wu & Tang, 2015
Illumination (use of light source)	Active	Passive (and Active)	Smith, M. W. & Quincey D. J., 2017
Instrument Costs	High	Low	Wu & Tang, 2015

3D Reconstructed Effort (complexity level and resource investment)	Medium	High	Telling, J., Lyda, A., Hartzell, P., & Glennie, C. (2017); Smith, M. W., Carrivick, J. L., & Quincey, D. J. (2016).

Photogrammetric compilations that rely solely on images typically do not provide significant challenges in terms of interpretation and thus can yield a rather high level of detailed texture (Jansa et al., 2004). In the event of inadequate texture, measurements may be utilised as an alternative means of analysis. There is a possibility of failure. Both limitations can be mitigated through laser technology (Jansa et al., 2004).

The fusion of CRP and LiDAR data is done to complement the qualities of both photogrammetry and LiDAR (Wu & Tang, 2015). The two types of datasets must be properly calibrated, registered, and analysed for them to provide reliable results. This project has four key concepts: the acquisition of data, fusion of LiDAR and CRP datasets, data registration and accuracy assessment.

Compared to CRP, LiDAR offers superior geometric accuracy and is largely unaffected by environmental factors such as lighting conditions and surface texture (Gašparović & Malarić, 2012; Rönnholm et al., 2007). Additionally,

LiDAR enables near-instantaneous 3D model reconstruction, whereas CRP can be labor-intensive due to the extensive processing required to align and interpret multiple overlapping images (Rönnholm et al., 2007).

A critical step in integrating LiDAR and CRP data for 3D model reconstruction is registration, which involves aligning the datasets. According to Haala and Alshawabkeh (2006), precise registration is essential for successful data integration. Misalignment can lead to inaccurate 3D reconstructions, resulting in flawed spatial information and unreliable decision-making. Achieving high-precision automated registration remains a challenge, as current procedures often require manual adjustments and refinements. Although practical methods are available, further development of more robust and computationally efficient registration techniques is necessary to improve data fusion accuracy.

Research has shown that LiDAR produces more accurate geometric models than CRP, making LiDAR point clouds a reliable foundation for refining photogrammetric 3D reconstructions (Rönnholm et al., 2007). In this fusion process, LiDAR provides precise spatial data, while CRP enhances the model by contributing high-resolution color and texture information. This involves extracting color values from registered CRP images and applying them to the LiDAR point cloud, improving both the visual and spatial quality of the final model.

Rönnholm et al. (2007) demonstrated this methodology by enhancing the visual appearance of LiDAR-generated models with photogrammetrically derived textures. Effective dataset alignment allowed the integration of both technologies' strengths, resulting in high-resolution, texturally accurate 3D models. This combined approach is particularly valuable for applications in underground mining and other complex environments, where both precision and detailed visualization are crucial.

One of the methods implemented to obtain reliable solutions is by thoroughly examining the camera calibration and dense point clouds (Luhmann et al*.,* 2020). A key factor in photogrammetry is the concept of registration, which produces a mathematical description of how the various images overlap. Image registration is the projection between two or more images captured by various sensors, at various times or from different views both geographically and in terms of intensity (Forkuo, 2005). Problems encountered with image registration can be revealed mathematically as shown in Equation 2.1 (Forkuo, 2005).

$$I_2 = (x', y') = g(I_1(T(x, y))) \quad (0.1)$$

Where: $I_1 \; and \; I_2$ are 2-dimensional images (indexed by x and y). T is a transformation that maps the two spatial coordinates x and y to two new spatial coordinates x^' and y^'. G represents one-dimensional intensity or radiometric transformations (Forkuo, 2005).

Image registration is done before integrating images and LiDAR datasets. This is because the translation and rotation of the camera must be determined relative to the LiDAR data (Forkuo, 2005). Image registration is essential for fusing data from different sensors and detecting image differences captured at different times (Hong & Zhang, 2007).

CRP alone can produce satisfactory texture quality for 3D models but there will always be complications when processing and assessing data (Haala & Alshawabkeh, 2006). However, when there is proper calibration of the LiDAR and CRP dataset, the captured images will be linked to the dense point cloud (Haala & Alshawabkeh, 2006).

2.4 Chapter Summary

According to the literature, there has been a drastic improvement in monitoring the FOG in underground mines. The two main methods used to improve safety in underground mines include remote sensing and contact technologies. Remote sensing technologies provide the benefit of acquiring data without requiring direct physical interaction with the location from which data is collected.

Remote sensing technologies have advantages over contact technologies including data acquisition without direct contact with the location where data is collected. Remote sensing technologies such as LiDAR and CRP are essential for monitoring rock deformations in underground mines. This enables the execution of necessary precautionary measures to enhance

safety including the implementation of necessary support before any unintended occurrence of FOG.

The integration of LiDAR and CRP complements the individual weaknesses of both remote sensing technologies. LiDAR has better geometric accuracy whereas CRP has sufficient texture of the underground mine workplace to be reconstructed. The four essential concepts when integrating LiDAR and CRP datasets are data acquisition, fusion of LiDAR and CRP datasets, data registration and accuracy assessment. When these four concepts are carefully considered, integrating the two remote sensing technologies can provide a comprehensive, holistic reconstructed 3D model.

3 RESEARCH METHODS

3.1 Steps Undertaken to Integrate LiDAR and CRP

The integration of LiDAR and CRP data is crucial for ensuring accurate calibration, registration and statistical analysis of the remote sensing technologies. However, a systematic approach must be followed to combine LiDAR and CRP. LiDAR data can be used as absolute controls to enhance the precision of photogrammetric analysis of underground mines.

Figure 3.1 presents the approach employed for data acquisition and reconstruction of 3D models using CRP, LiDAR and fusion of the two remote sensing technologies.

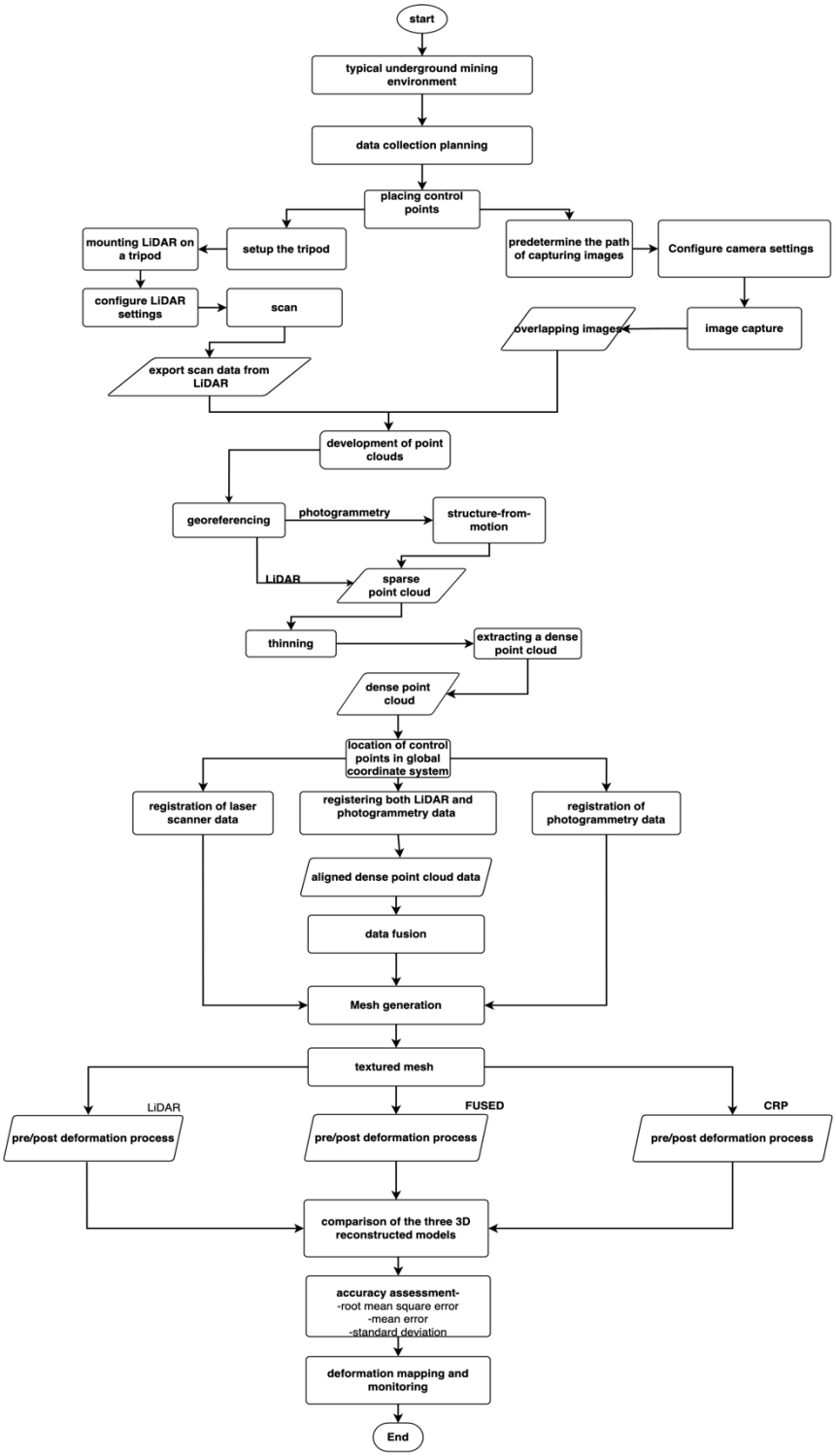


Figure 3.1: The fusion of LiDAR and CRP to reconstruct a photorealistic 3D model.

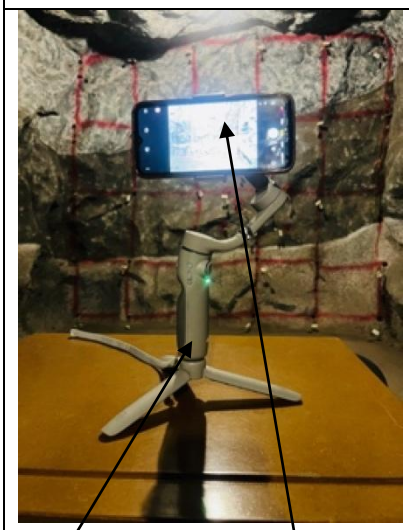
Forkuo (2005) outlines numerous procedures that can be executed to provide an accurate 3D reconstructed model by fusing LiDAR and CRP datasets, which serve as the foundation of the methodology in this research. These steps include:

1. Dataset acquisition: data was collected from both LiDAR and CRP under the same coordinate system. This is because the workplace is a 3D domain (x, y, and z extents) therefore any coordinate projection should be under the same coordinate system including georeferenced images (Jiang et al., 2022).
2. Data pre-processing: there are necessary steps that were done to pre-process data. These are:
    i. Data cleaning and enrichment: removing irrelevant data such as duplicates and collecting missing data. Irrelevant data might include scans and images that are not part of the preferred area of analysis;
    ii. Data transformation: ensuring the datasets obtained align with the goal of the research; and
    iii. Data validation: checking the captured data's quality and accuracy (Lawton, 2022).
3. Data overlapping: this is when the existing data was recaptured at a certain percentage. Images overlap at a percentage of 80% in CRP. LiDAR scans also overlap due to scan locations being closer to each other. This ensured better registration of data for both LiDAR and CRP techniques.

4. Dataset merging: integrating data from photogrammetry and LiDAR using appropriate software fit for the purpose.
5. Alignment of datasets: datasets were aligned using different methods such as accuracy analysis and visual inspection (Forkuo, 2005).

The equipment used for data collection using both LiDAR and CRP techniques in this research is shown in Table 3.1.

Table 3.1: Main components used for data acquisition to reconstruct 3D models of Wits Mock Mine.

Field System Components	
Photogrammetry Components	**LiDAR Components**
	

DJI Osmo stabilising gimbal

Android device (Samsung A14)

Laser scanner

Tripod

Handheld Controller

3.2 Photogrammetry Components and their Parameters

3.2.1 DJI Osmo Stabilising gimbal

Nocerino and others focused on the impact of image stabilisation (IS) on 3D models reconstructed using the photogrammetry concept (Nocerino et al., 2022). According to the literature, using internal orientation for IS is not the best approach for photogrammetry (Nocerino et al., 2022). This is because it affects the sharpness of images which is one of the most essential factors for a reliable photogrammetric reconstructed 3D model.

This research focused more on stabilising the exterior factors thus avoiding distortion of images. The stabiliser software application, DJI Mimo, was installed on the Samsung A14 device to enhance its stability when capturing images for photogrammetry.

3.2.2 Android device

Samsung A14 is a cost-effective equipment employed for CRP in this research. The Android device comprises triple main camera sensors and an LED flashlight essential for CRP especially in low-lit environments. Table 3.2 shows the main camera sensors' features.

Table 3.2: Megapixels and apertures of the triple main camera sensors of Samsung A14 device.

	Camera quality	Aperture
Camera 1	50 MP	f/1.8 (wide)
Camera 2	5 MP	f/2.2 (ultrawide)
Camera 3	2 MP	f/2.4 (macro)

Camera 1 is the primary camera utilised due to its inclusion of phase detection autofocus (PDAF), which allows the sensor to rapidly and automatically focus. A PDAF sensor comprises two photodiodes, with each photodiode receiving light from one half of the lens (Jutamulia, 2022). This can be illustrated in Figure 3.2 where two images of the same object are shown. Autofocus is attained by comparing the light received by both photodiodes in the PDAF sensor (Jutamulia, 2022).

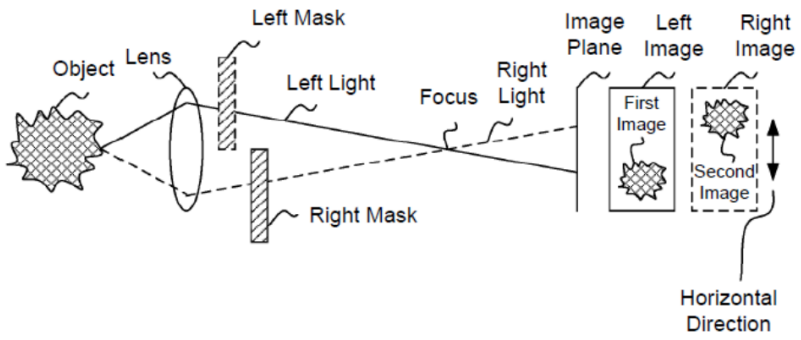


Figure 3.2: Principle of PDAF (Jutamulia, 2022).

Camera sensors had drawbacks, including delay in image capture in low-lit environments. One of the main reasons is that low light can be recognised as high noise in camera sensors because it affects the resolution and colour accuracy of images (Peltoketo, 2015).

One of the main parameters encountered when collecting data in underground mines was low lighting conditions which mainly affected the photogrammetric collection of data. Therefore, to overcome this limitation a flashlight on the Android device was always switched on to capture detailed images of the Wits Mock Mine.

3.2.3 Photogrammetry Equations

To explain the perspective of a camera, three coordinate systems are needed which include the camera coordinate system, the 3D objects coordinate system and the 2D image coordinate system (Schindler, 2015). These coordinate systems are represented by $\tilde{x}$, X and x respectively.

The transposition of a matrix is represented as X^T and the cross-product of two 3-vectors is shown in two ways. It can be represented either as x * y or $[x]_\times y$ such that when x = [u, v, w]^T, Equation (3.1) is applied.

$$[X]_x = [0\ -w\ v\ w\ 0\ -u\ -v\ u\ 0\ ] \tag{3.1}$$

Equation (3.2) shows the Kronecker product between two vectors or matrices.

$$X \otimes Y = [x_{11}Y\ x_{12}Y\ \ldots\ x_{1n}Y\ x_{21}Y\ x_{22}Y\ \ldots\ x_{2n}Y\ \vdots\vdots\ddots\vdots\ X_{m1}Y\ x_{m2}Y\ \ldots\ x_{mn}Y\ ]$$

(3.2)

Equation (3.3) refers to a 3D object point with Euclidean coordinates $\frac{1}{T}$ [U, V, W]^T such that when T is not equal to zero, it is the projective scale squared (Schindler, 2015).

$$X = [U, V, W, T]^T \tag{3.3}$$

Similarly, a 2D image point is illustrated in equation (3.4).

$$x = [u, v, t]^T \tag{3.4}$$

Equation (3.5) shows the perspective mapping from camera coordinates to image coordinates (Schindler, 2015).

$$x = [O]\tilde{x} = \ [c\ 0\ x_H\ 0\ 0\ c\ y_H\ 0\ 0\ 0\ 1\ 0\ ]\tilde{x} \tag{3.5}$$

Equation (3.5) only applies when the image coordinate system has no shear and isotropic scale. This is because the camera projection matrix which is obtained from the extrinsic and intrinsic parameters of the camera becomes less complicated because additional transformations are not required (Hartley & Zisserman, 2003).

When there is shear (s) and a scale difference (m), the camera matrix would be as shown in equation (3.6) which also shows all the five parameters for interior orientation (Schindler, 2015).

$$K = [c\ cs\ x_H\ 0\ c(1+m)\ y_H\ 0\ 0\ 1\ ] \tag{3.6}$$

The projection matrix is used to obtain exterior and interior parameters (Schindler, 2015). This is illustrated in equation (3.7) (Schindler, 2015).

$$P = [M|m] = [KR| - KRX_0^e \tag{3.7}$$

The external orientation's translation component is obtained from equation (3.8).

$$X_0^e = -M^{-1}m \tag{3.8}$$

Equation (3.9) is applied to recover the rotation, translation, and scaling photogrammetric problem. Object coordinates are obtained from model coordinates.

$$X = SRTX^m = \left[\frac{1}{s}I\ 0\ 0^T\ 1\ \right][R\ 0\ 0^T\ 1\ ][I\ -T\ 0^T\ 1\ ]X^m \tag{3.9}$$

Where: X^m is coordinates of the angle preserving photogrammetric model.

Six exterior orientations and five interior orientations that complete the orientation of one image are unknown (Schindler, 2015). Equation (3.10) indicates Direct Linear Transform (DLT) which is an algebraic solution.

$$[x]_{\times}PX = ([x]_{\times} \otimes X^{T})p = 0 \quad (3.10)$$

Where: p = vec (P) = $[P_{11}, P_{12}, \ldots., P_{34}]^{T}$.

The main aim of these algorithms in photogrammetry is to reconstruct a 3D model, which can only be obtained through triangulation (Schindler, 2015). The triangulation was implemented from camera object points with known orientations P_i. Each image point gives rise to equation (3.11) (Schindler, 2015). This equation is a good estimation when proper numerical conditioning is done.

$$([x_i]_x P_i)X = 0 \quad (3.11)$$

To ensure proper numerical conditioning, it is of paramount importance to choose appropriate numerical algorithms and representations of data. Camera orientations are always a by-product even when the main objective was to reconstruct a 3D model for deformation mapping and monitoring.

3.3 LiDAR Components and their Parameters

3.3.1 Terrestrial Laser Scanner

The terrestrial laser scanner used in this research is Maptek I-Site 8800 with a range of up to two kilometres. The field of view is 360 degrees horizontal and 80 degrees vertical (Maptek, 2012). A Panasonic FZ-G1 touchpad is connected to the terrestrial laser scanner using an ethernet cable and provides essential features necessary to extract the 3D models.

The terrestrial laser scanner consists of Inertial Measurement Unit (IMU), laser pointer, a camera and a range finder. IMU is a component of LiDAR that provides orientation and motion data to the laser scanning device (Raval et al., 2019). It achieves these objectives because it is equipped with three sensors which are:

- Gyroscopes: it measures the angular rate on the x, y and z axes (Ahmad et al., 2013).
- Accelerometers: sensors that measure the location and speed of the laser scanner along the x, y and z axes (Ahmad et al., 2013).
- Magnetometers: the sensors ensure the gyroscope sensors accurately determine the absolute orientation by measuring the intensity and direction of the magnetic field (Ahmad et al., 2013).

3.3.2 Tripod

A tripod was one of the most important equipment in this research because of the following reasons:

- It enhanced LiDAR equipment's stability, hence increasing the precision of the 3D model. This is achieved by preventing vibrations and swaying of LiDAR sensors in the underground mining environment.
- A tripod greatly impacts the LiDAR sensors' angle and orientation to collect consistent and dependable data.
- A tripod provided security for the LiDAR instrument, which is both large and heavy.

- It also ensured the laser scanner can easily be placed in various positions in the underground environment.

3.3.3 Hand-Held Controller (HHC)

The HHC was used to collect data scanned by the LiDAR equipment. It comprises of a pen to input necessary data and a colour graphical interface. The input function shown on the HHC is utilised to provide several factors required for scanning data such as the ambient temperature, current location of the scanner and the observed backsight prior to scanning. The HHC was also used to select the specific location that has to be scanned from a preview scan. Its sole purpose was to direct the operation of the Maptek I-Site 8800 scanner used in this research.

3.3.4 LiDAR Equations

The LiDAR was calibrated to minimise systematic inaccuracies in the acquired point cloud and the user implemented it to access current, high-quality information. Holst et al. (2016) illustrate that it is better to use polar coordinates instead of using Cartesian coordinates because they are better suited for field measurements. Some surveying equipment such as a total station measure the horizontal angles and distances which align with polar coordinate system. One of the proposed models which is the systematic error model illustrates equation (3.12) (Holst et al., 2016):

$$\delta r_i^j = a_0 + a_1 r_i^j + a_2 sin\theta_i^j + a_3 sin\frac{4\pi r_i^j}{u_1} + a_4 cos\frac{4\pi r_i^j}{u_1} + a_5 \, sin \, sin\frac{4\pi r_i^j}{u_2} + a_6 cos\frac{4\pi r_i^j}{u_2} + a_7 sin4\varphi_i^j + a_8 cos4\varphi_i^j \quad (3.12)$$

Where: r_i^j is distance, φ_i^j is an angle about the secondary rotation axis and θ_i^j is the angle about the primary rotation axis. $U_1\ and\ U_2$ are the shortest and second shortest modulation wavelengths.

Other existing models include iterative closest point (ICP) calibration, intensity-based calibration, and plane-based calibration. The systematic error model was chosen because of the application requirements and the nature of the LiDAR used.

Equations (3.13) and (3.14) illustrate how the laser scanning coordinate system and the camera system coordinate systems are transformed into the global coordinate system, which is usually the coordinate system of a national reference system.

$$x_{GLCS} = M_{POP} M_{SOP,n} x_{SOCS,n} \tag{3.13}$$

$$x_{GLCS} = M_{POP} M_{SOP,n} M_{COP,n,m} M_{mount}^{-1} x_{CMCS,n,m} \tag{3.14}$$

Where: SOCS is the scanner's coordinate system, CMCS is the camera coordinate system and GLCS is the global coordinate system. $M_{POP}\ and\ M_{SOP}$ are matrices that show the changes from raw laser data to global coordinate systems via the project coordinate system (Jansa et al., 2004).

The majority of LiDAR equipment is classified as IP65, indicating that it is both dustproof and resistant to humidity (Maptek, 2012). Nevertheless, it is

advisable to avoid subjecting the instrument to prolonged exposure to humid climatic conditions, since this might result in significant moisture infiltration that may adversely impact the instrument (Maptek, 2012).

3.4 Wits Mock Mine

The images collected using a camera were imported into photogrammetry software, MicMac, and reconstructed into a 3D model using fit-for-purpose algorithms. CRP produces 3D models that are accurate, precise and of high resolution depending on several variables, such as the range between the camera and the object, the camera and lens employed. Mine safety also has an effect on the accuracy regarding the allowable distance from a face and the roof support as per regulations and the mine standards.

Collecting data in actual underground mines can be extremely challenging due to the necessary protocols for mine access, safety measures when integrating new technology and privacy regulations enforced by the mine. A significant portion of time is typically allocated to getting to the mine site and conducting screening activities before descending underground to gather data. Mining shifts may impose time constraints that disrupt the data-collecting process.

This research focuses on the research conducted at the Wits Mock Mine, situated within the African Rainbow Minerals (ARM) building on the west campus of the University of the Witwatersrand in Johannesburg, South Africa. Most of the simulated features in Wits Mock Mine closely resemble

those seen in underground mines. This includes materials used to construct Wits Mock Mine which are primarily identical to those commonly found in underground mines.

The Wits Mock Mine replicates the many parts commonly found in underground mines such as the stope panel, refugee bay, tunnel and lamproom. It is equipped with cutting-edge technologies that can be utilised in actual underground mining operations. The tunnel spans a length of 67 meters and exhibits changing width from the blasting face to the opposite end. The tunnel is comprised of reefs and faults along with a ventilation pipe and gas detection instrumentation (GDIs) positioned close to the blasting face.

Several research experiments were carried out in the Wits Mock Mine due to its inclusion of several factors that most accurately represent the conditions found in an underground mining environment. This includes the study conducted by Ashraf et al. (2022) which involved a numerical evaluation of the specific absorption rates (SAR) in the human head and torso. The parameters are detected by using wearable electronics in a simulated mine environment at Wits Mock Mine. The feasibility of numerically evaluating SAR in underground mines was addressed due to the potential impact of radiofrequency field levels in limited spaces.

An investigation in the Wits Mock Mine successfully utilised wireless sensor networks (WSNs) to locate sensors buried under 20 kg gravel bags

(Mahmood et al., 2024). The main objective behind the research was to detect the missing miner in a collapsed underground mine thus the potential for saving lives (Mahmood et al., 2024).

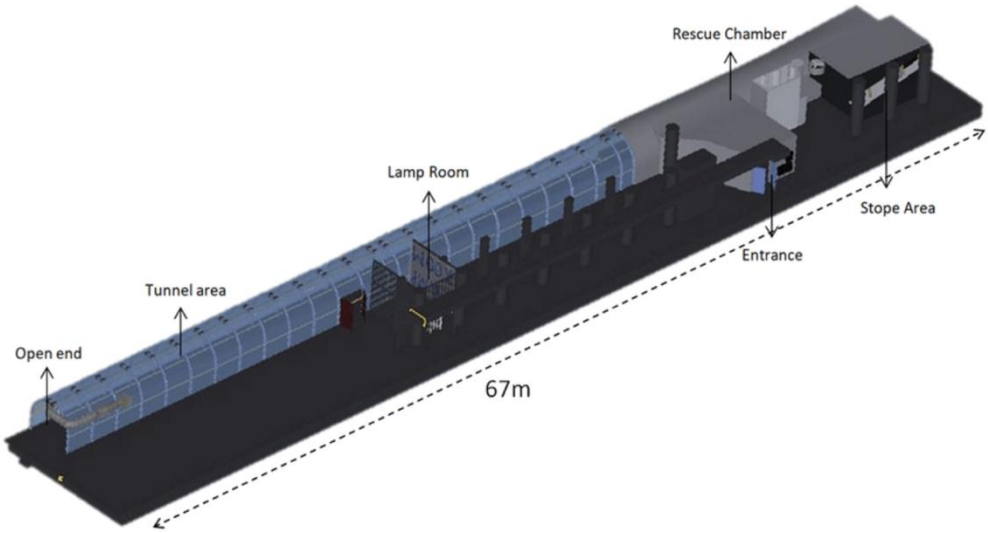


Figure 3.3: 3D model of a Wits Mock Mine used to illustrate the locations of the tunnel, stope panel and lamp room (Zaman et al., 2018).

The Wits Mock Mine is equipped with strategically placed ground control points (GCPs) to facilitate remote sensing data acquisition, allowing for a comprehensive overview of the Wits Mock Mine.

3.5 Research Design

Two possible methods were used to align LiDAR and CRP point clouds. This includes the use of 3D Gizmo tool and control points. 3D Gizmo has many functions that include: scaling, rotating and translating models. The tool aligns LiDAR point clouds by using a related checkbox, an option that allows the selection of all required sections of the model for alteration. Modification of model alignment can be improved by providing a uniform color, which makes it easier to align point clouds.

GCPs are specific locations with predetermined coordinates used to align accurately and reference datasets obtained from geospatial and mapping endeavours. They are mainly used in photogrammetry, surveying and other remote sensing technologies. GCPs impact the precision of deformation analysis (Jiang et al., 2022).

To match reconstructed 3D models to real-world coordinate systems, LiDAR and CRP technologies employ GCPs. GCPs are crucial in this study since they directly influence the precision of the deformation analysis on the reconstructed 3D models.

A minimum of three GCPs can be sufficient to accurately reconstruct a 3D model of the Wits Mock Mine environment using LiDAR and CRP (Taufik & Puspitasari, 2019). These GCPs should be strategically positioned to ensure LiDAR and CRP sensors capture the overall Wits Mock Mine tunnel. GCPs are also used when aligning and georeferencing image captures for photogrammetry (Taufik & Puspitasari, 2019). Therefore, to ensure the

smooth alignment of scans, it is advisable to ensure GCPs are visible when scanning.

3.6 Data Collection Process

The selection of several objects to depict post-deformation was based on their varied geometric characteristics, colour, texture and other aspects outlined in Table 3.4. A range of parameters were implemented to assess the best approach to be executed due to the many challenges encountered in underground mining. These objects were used in this research to simulate deformation that occur in actual underground mines.

Table 3.3: Objects positioned in Wits Mock Mine to depict post-deformation conditions and the justifications for simulating these objects.

	Objects	Parameters
1. Spherical paper		It is visible and highly recognisable thus it can easily be detected by both LiDAR and CRP technologies. The spherical structure of the object is used to simulate uniform deformation in underground mines.
2. Plastic cup		Varying geometries of the cup can test both LiDAR and CRP technologies' ability to distinguish non-uniform structures. The brown paper surrounding the cup tests photogrammetry technology's ability to obtain detailed surface features.

3. Plastic plate		Ideal for testing LiDAR and CRP on planar deformations. It can represent surface subsidence and bulging of rocks.
4. Pencil		Ideal for testing both LiDAR and CRP on narrow objects. It depicts small changes that happen in underground mines.
5. Cylindrical container		The object was chosen to test how the remote sensing technologies can handle circular cross-sections. The two different colours of the object provide different reflectivity thus assessing how LiDAR and CRP respond to different surfaces.
6. Concrete Rock		It simulates actual material found in underground mines. Because of its varying geometries, the rock is a good test on how both LiDAR and CRP can map non-uniform changes.
7. Fluorescent tube		An elongated object which depicts structures like support beams. It is useful to test varying lighting conditions in underground mines.

8. Brick		It is used to test how LiDAR and CRP technologies define sharp edges and corners. The object reviews a real scenario for monitoring tilts in underground mines.

The equipment used as a conventional way to collect geometric measurements is a tape measure which is shown in Figure 3.4.



Figure 3.4: Tape measure used for conventional measurements of varying components in the Wits Mock Mine tunnel including objects indicating post-deformation properties.

3.8 Chapter Summary

This chapter examines the methodology employed for data collection in this research. The research seeks to encompass all various limits faced in operational underground mines and examines appropriate strategies to acquire precise datasets essential for deformation monitoring and mapping. This chapter illustrated the equipment utilised for both LiDAR and CRP principles. LiDAR data can serve as absolute controls to enhance the

accuracy of photogrammetric processing in a typical underground mining environment. The research was conducted at the Wits Mock Mine, located within the African Rainbow Minerals (ARM) facility on the west campus of the University of the Witwatersrand in Johannesburg, South Africa. The simulated features of the Wits Mock Mine closely mirror those observed in underground mines.

4 DATA FOR THE STUDY

Monitoring deformation in the underground mine with high accuracy significantly improves safety of mine personnel. The accuracy of deformation being mapped and monitored depends with the datasets being used. High quality data for this research is used to accurately monitor deformation and assess the accuracy of results obtained. LiDAR and CRP datasets are suitable to achieve the objectives of this research. This chapter explains how data was analysed to ensure it is fit-for-purpose.

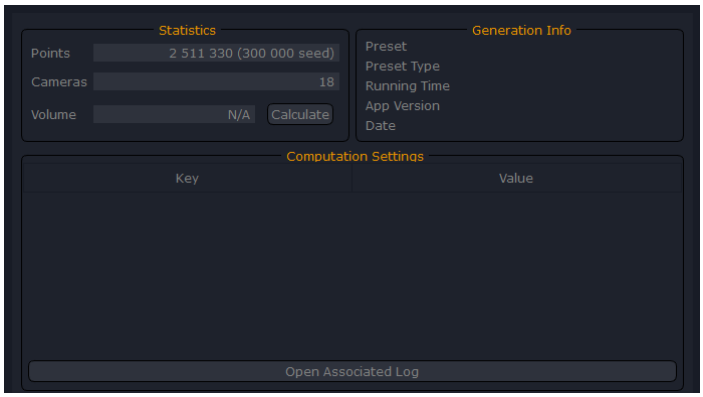
4.1 Point Cloud Density

The density of point clouds is an important factor that influences the precision of 3D models in applications such as deformation monitoring. Point cloud density, typically measured in points per square metre, determines the level of detail obtained in the reconstructed 3D model (Shan & Toh, 2018). Point cloud density is adjusted depending on the main reasons behind reconstructing the 3D models. Higher point cloud densities enable the ability to view smaller features and finer resolution, while lower point cloud densities fail to spot the subtle features that might be relevant in high-precision research (Berger et al., 2017).

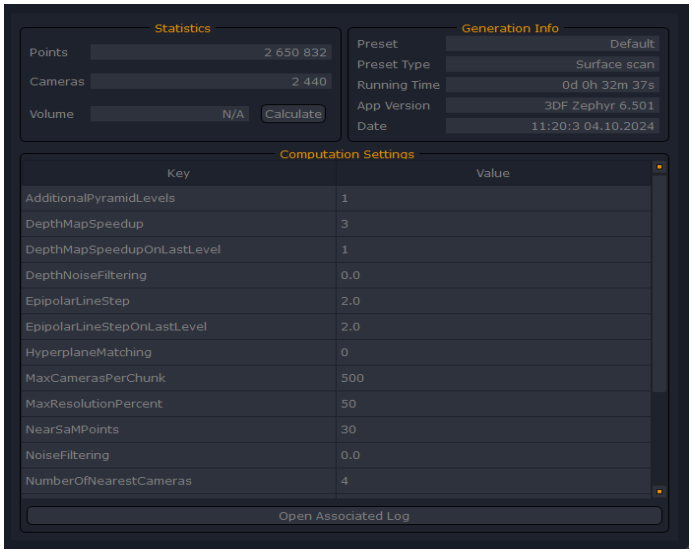
Ensuring consistency of point cloud densities is critical when combining LiDAR and CRP to avoid biases and inconsistencies in the model (Guidi et al., 2009). The accuracy can be affected by the disparities in the point cloud density of the combined model. Therefore, ensuring that the final output

consists of almost equal point cloud densities by reducing the size of the point cloud improves the robustness and accuracy of the fused model. This process is known as decimation.

During the pre-deformation phase, the LiDAR point clouds were reduced from 10,045,321 points to 2,511,300 points, as illustrated in Figure 4.1a. The dense point cloud for CRP in the pre-deformation comprises 2,650,832 points, as illustrated in Figure 4.1b. The MicMac software facilitated this approach.



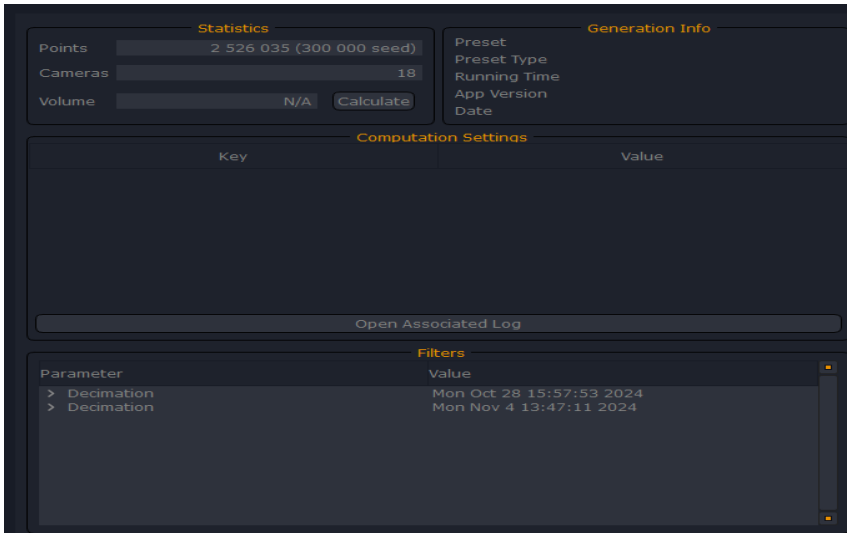
a)



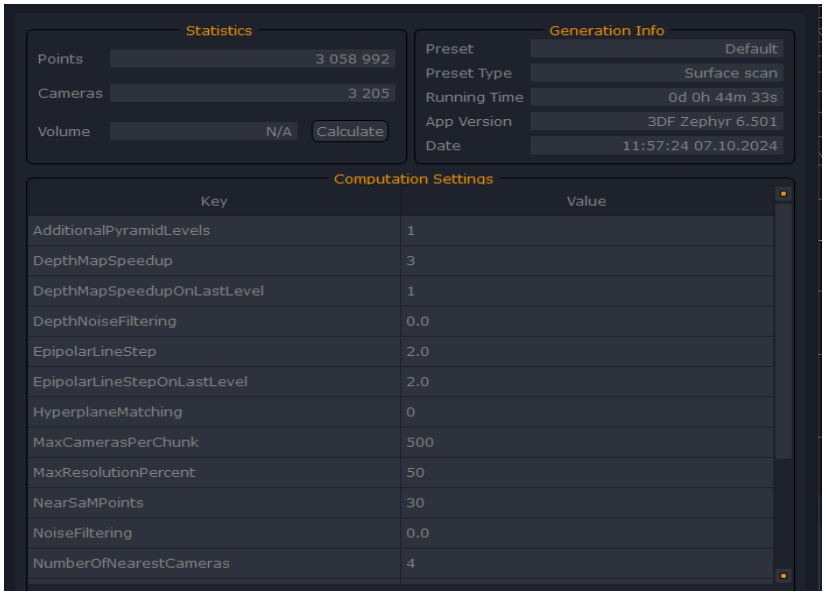
b)

Figure 4.1: Indication of the number of points in the pre-deformation stage of a) decimated LiDAR point cloud model and b) CRP point cloud model.

During the post-deformation process, the initial number of points obtained using LiDAR was 10 104 143 points which was decimated to 2 526 035 points which is more uniform with CRP points with 3 058 992 points. This procedure is illustrated in Figure 4.2.a) and Figure 4.2 b).



a)



b)

Figure 4.2: Decimation of LiDAR point cloud in post-deformation to ensure there is consistency of point clouds between a) LiDAR and b) CRP point clouds.

The feature size for pre-deformation and post-deformation 3D models was calibrated to range from 0.010m to 0.050m for LiDAR point clouds. This is advantageous for preservation and file size management during processing and analysing while optimising the necessary details. Feature size denotes the resolution level primarily influenced by point cloud density.

Consequently, increased point cloud density facilitates the assessment of minor alterations, such as rock fractures and displacement. However, this will necessitate additional time and computational resources; hence, such considerations were incorporated into the data pre-processing phase. The specified parameters are sufficient at predicting any failures and thereby preserving lives. Safety is upheld and hazards are maintained at a reasonable level.

4.2 Compatibility of Collected Data

Data used in this research was analysed to ensure that it is fit-for-purpose for this research. In a typical underground mining workplace, deformation can occur anywhere due to various factors such as vibrations occurring underground and other mining operations. Therefore, to ensure FOGs are well-monitored and will not result in fatalities and injuries of mine personnel, the whole mine has to be monitored. Data collected using both LiDAR and CRP technologies had a perfect coverage thus ensuring the data is relevant to the study area.

The data utilised in this research aligns with its objectives, as LiDAR technology acquires high-resolution scans, while CRP captures surface and spatial features crucial for deformation analysis. Accuracy assessment can be derived from data collected and has a potential of being enhanced by integrating remote sensing technologies, which can improve surface characterisation.

There is temporal relevance of data from both LiDAR and CRP technologies, because the datasets are obtained in both pre-deformation and post-deformation stages. This allows for comparison and validation of data before analysing deformation.

Data collected suffices the objectives of the research. Multiple scans were achieved using the LiDAR technology in both pre-deformation and post-deformation stages. Multiple images were also captured using the CRP technique thus ensuring enough data can be used for analysis. The amount of data collected is explained in Chapter 5.

The suitability of LiDAR and imagery sensors in this research lie solely on the ability to fuse them and assess the accuracy of the reconstructed 3D models. Accuracy assessment of the reconstructed 3D models provides certainty of the ability to monitor deformation.

4.3 Chapter Summary

This chapter focused on the type of data used for 3D model reconstruction including to what extent it can meet the objectives of this research. The main objectives of this research include fusing LiDAR and CRP datasets, accuracy assessment of the 3D models and monitoring deformation in a typical underground mining environment. This data excluded use of GPS because GPS cannot penetrate in the underground mining environment.

There are two main factors that play a huge role to determine the feasibility of the collected data. These include qualitative and quantitative factors, which can provide a more holistic approach when monitoring deformation and assessing the accuracy of the reconstructed 3D models. These factors are imperative and were taken into account when choosing the to monitor deformation in underground mines.

Density of point clouds can be adjusted to meet the requirements of the research. Some of the parameters include ensuring equivalent density of point clouds from both LiDAR and CRP to avoid bias from either datasets.

5 RESULTS AND DISCUSSION

5.1 Introduction and Objectives of the Analysis

Deformation monitoring using conventional methods poses threats to human safety. Mine personnel conducting measurements must physically access the hazardous workplace where deformation occurs, which may pose safety risks. Therefore, it is beneficial to implement systems that not only eliminate direct contact with a hazardous workplace but also improve the accuracy of monitoring deformation in underground mines. Necessary precaution measures would then be undertaken at the identified hotspots before any hazardous incidents occur.

The accuracy of spotting the hotspots where rockfalls are most likely to occur is paramount. This research focused on different dimensions of objects that depict different sizes of rocks or movements that may have occurred in underground mines as deformation.

During this procedure, different results were analysed using parameters mostly found in underground mines. The results of the CRP and LiDAR techniques and the combination of the two techniques were compared to the traditional method which is use of a tape measure. The research characterises post-deformation in the Wits Mock Mine as a phase in which objects are placed within the tunnel. This situation demonstrates the temporal alterations that occur in underground mines when deformation occurs gradually over time before a rockfall.

This chapter examines the extent to which combined CRP and LiDAR technologies significantly improve deformation monitoring in underground mines. This chapter also assesses the potential of integrated CRP and LiDAR to enhance several facets of underground mining operations. The research excluded the processing time for reconstructing 3D models, as the primary objective was to integrate the two technologies, monitor deformation and conduct an accuracy assessment. This chapter emphasises the key factors that influence the precision of integrated CRP and LiDAR technologies.

5.2 Data Acquisition and Registration of Point Clouds

5.2.1 Registration of LiDAR point clouds

Three scans were acquired using LiDAR technology. The LiDAR equipment was positioned beneath three designated survey pegs to guarantee comprehensive coverage of the tunnel for investigation. The LiDAR equipment was positioned under pegs t2, t4 and t8. Figure 5.1 shows how the LiDAR equipment was positioned under each survey peg. A tape measure was attached to the survey peg to ensure that LiDAR was positioned correctly. Appendix A and Appendix B illustrate how data was collected using LiDAR before processing.



Figure 5.1: Illustration of how LiDAR was positioned under each peg in the Wits Mock Mine.

The LiDAR equipment has a minimum operational range of 1.5 metres and a maximum range of two kilometres (Maptek, 2012). Three LiDAR scans may overlap to compensate for missing data in one of the scans. Multi scans provide a full coverage of the Wits Mock Mine thus capturing complex geometries. Figure 5.2 illustrates the data gap. The data gap arises from the limitations inherent in the line of sight of LiDAR technology. The LiDAR point clouds were initially generated using Maptek Pointstudio software, which facilitated data visualisation before integration with CRP data.

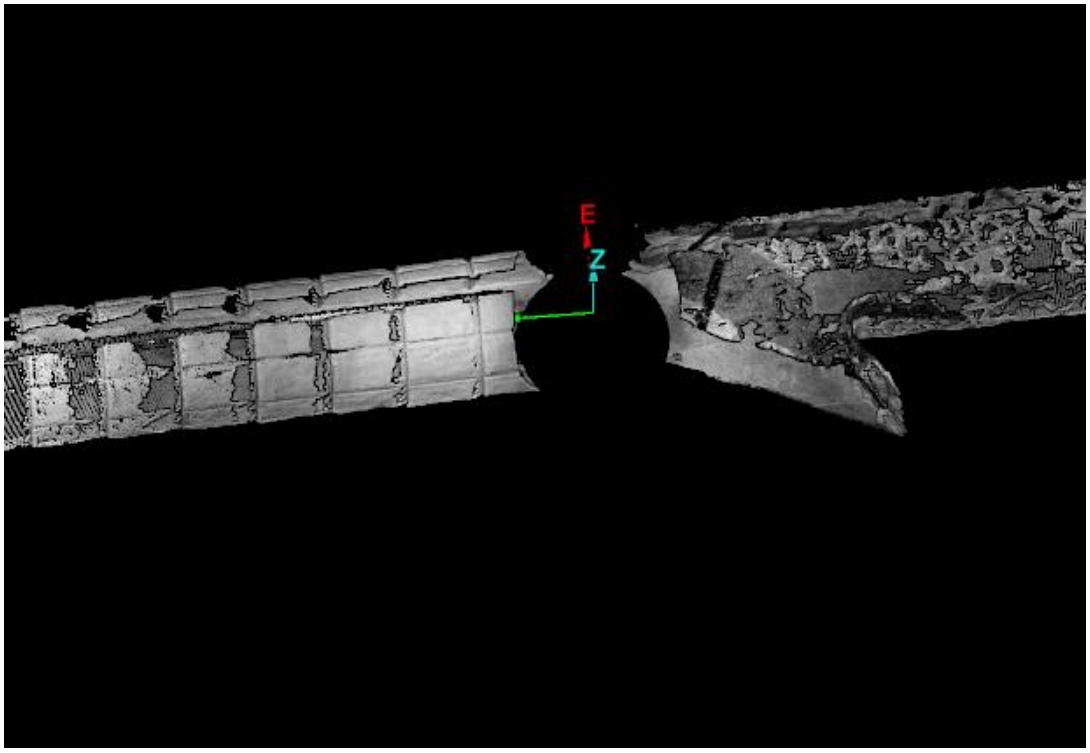
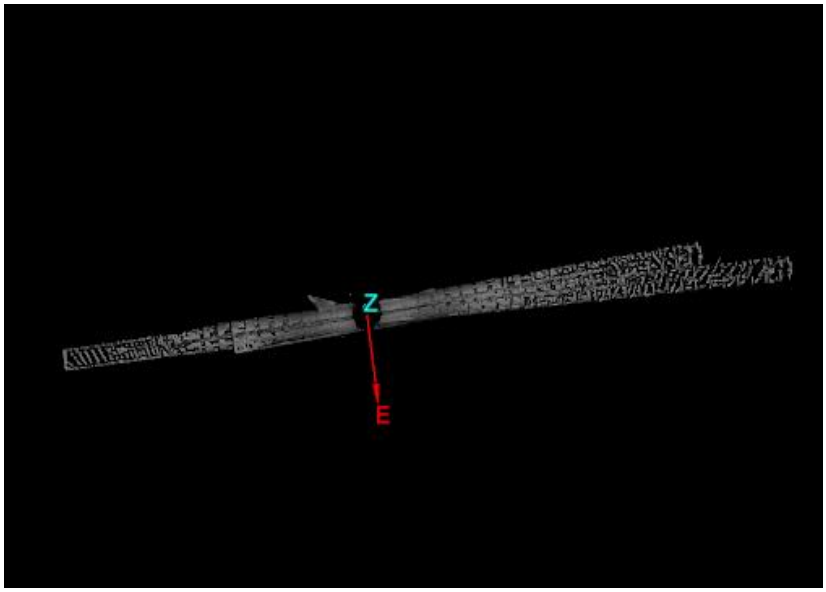
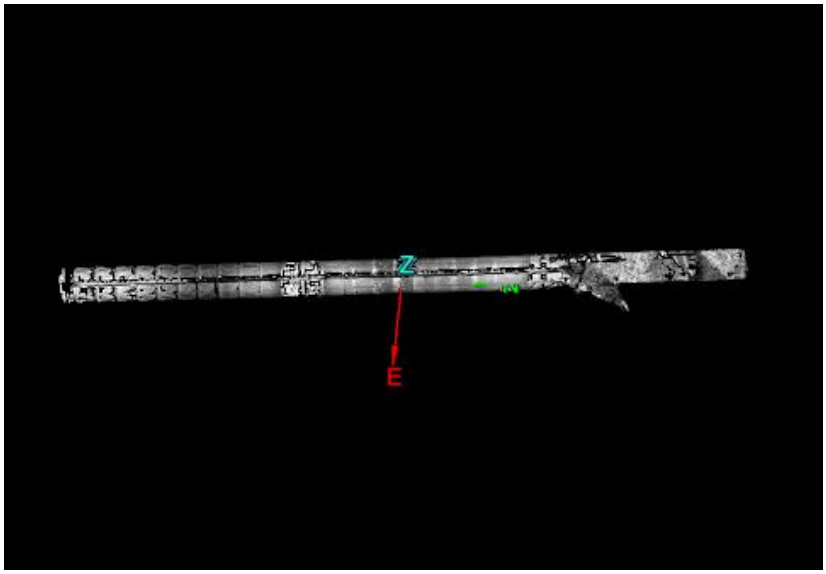


Figure 5.2: Missing data observed in one of the LiDAR scans of Wits Mock Mine.

The same principle was applied in both the pre-deformation and post-deformation stages of scanning. Once the scans from both pre-deformation and post-deformation were registered, the LiDAR point clouds were georeferenced. The point clouds were individually geo-referenced before fusing them to ensure better alignment of point clouds from both CRP and LiDAR models. Figure 5.3 shows the scans before and after they were registered, which is change in position of the 3D model to a known point with known coordinates. After registration, the 3D model is then geo-referenced.



a)



b)

Figure 5.3: Illustration of (a) unregistered LiDAR scans and (b) registered LiDAR scans.

5.2.2 Registration of CRP Point Clouds

The alignment of images in Close-Range Photogrammetry (CRP) model reconstruction is governed by various algorithms that optimise the registration process to enhance model accuracy. These algorithms play a crucial role in ensuring precise alignment of overlapping images, improving spatial consistency and minimising reconstruction errors. Enhancing the performance of these alignment algorithms can significantly increase the reliability of 3D models, particularly in environments with complex geometries or challenging conditions.

a) Feature Detection Algorithm (SIFT)

The feature detection algorithm used in this research is the Scale-Invariant Feature Transform (SIFT). The algorithm checks the main common points found in images thus accommodating other applications such as model reconstruction and image matching (Karami et al., 2017). The algorithm detects distinctive spots, such as corners, that can be aligned along with other captured images. Table 5.1 shows a python code executed for detecting unique points in CRP.

The numpy library, illustrated in the python code in Table 5.1, is imported because it solves complex mathematical equations whereas cv (computer vision) library is used for image processing. It should be noted that the main objective of this code is to detect the key points in the grayscale and then of the original image.

Table 5.1: Illustration of the code implemented in the SIFT feature detection algorithm (OpenCV, 2024).

import numpy as np
import cv2 as cv
img = cv.imread('home.jpg')
gray= cv.cvtColor(img,cv.COLOR_BGR2GRAY)
sift = cv.SIFT_create()
kp = sift.detect(gray,None)
000img=cv.drawKeypoints(gray,kp,img)
cv.imwrite('sift_keypoints.jpg',img)

Additional feature detection methods encompass Speeded-Up Robust Features (SURF) and Oriented Fast and Rotated Brief (ORB). SURF is less effective than SIFT, although it is faster due to its use of integral images for pre-processing data. ORB is not as accurate as SIFT and SURF and is typically employed in real-time applications.

b) Image Matching Algorithm (Ransac)

The image imatching algorithm is employed for feature detection, primarily to eliminate outliers that do not correspond with the required features (Verykokou & Ioannidis, 2018). The Random Sample Consensus (RANSAC) algorithm is used to verify point correspondence during 3D model reconstruction, as these points are critical for the precision of geometric measurements related to camera positioning (Paar & Bauer, 2005). It randomly selects point samples and executes the transformation.

c) Bundle Adjustment

Bundle Adjustment is a process used to refine the reconstructed 3D model thus enhancing its accuracy. The accuracy of the model is enhanced by optimising the positions of points and the camera orientation. Once the 3D points are correctly positioned, the reprojection error upon all images is reduced. The algorithm determines the alignment of the reconstructed 3D model by ensuring there is consistency across the images captured in the Wits Mock Mine.

d) Camera Calibration

The quality of the camera plays a huge role when CRP 3D models are being registered. Image geometry is affected by the type of camera used because of its intrinsic parameters which include focal length, lens and camera stability when capturing images. Cameras can automatically correct any distortions of its images before processing ensuring the point clouds obtained from the images remain aligned.

e) Structure from Motion (SfM)

SfM algorithm is employed to ascertain various camera postures during the capture of 2D images and their reconstruction into a sparse 3D model (Verykokou & Ioannidis, 2018). It aligns the points into a common coordinate system and allows dense point cloud generation of the models (Atik & Duran, 2022).

Executing these algorithms when reconstructing 3D models using CRP in software can automatically register the 3D model. Figure 5.4 shows a registered 3D model reconstructed using CRP in the pre-deformation stage; the same principle was also applied in the post-deformation stage.



Figure 5.4: Registered point clouds in a reconstructed 3D model of the Wits Mock Mine tunnel using the CRP principle.

5.3 Georeferencing in a Global Navigation Satellite System (GNSS)-Denied Underground Mine

Georeferencing of data is a crucial procedure in the reconstruction of an accurate geometrical 3D model. Satellites cannot penetrate the Earth's surface, rendering the collection of accurate spatial data in underground

mines difficult. Thus, a total station was utilised to collect data from the surface, where GNSS is available, and to transfer the coordinates into the Wits Mock Mine for survey peg installation. Figure 5.5 shows the survey pegs with designated GCPs used in this research. The positioning of the pegs on the reconstructed models is shown later in this section.

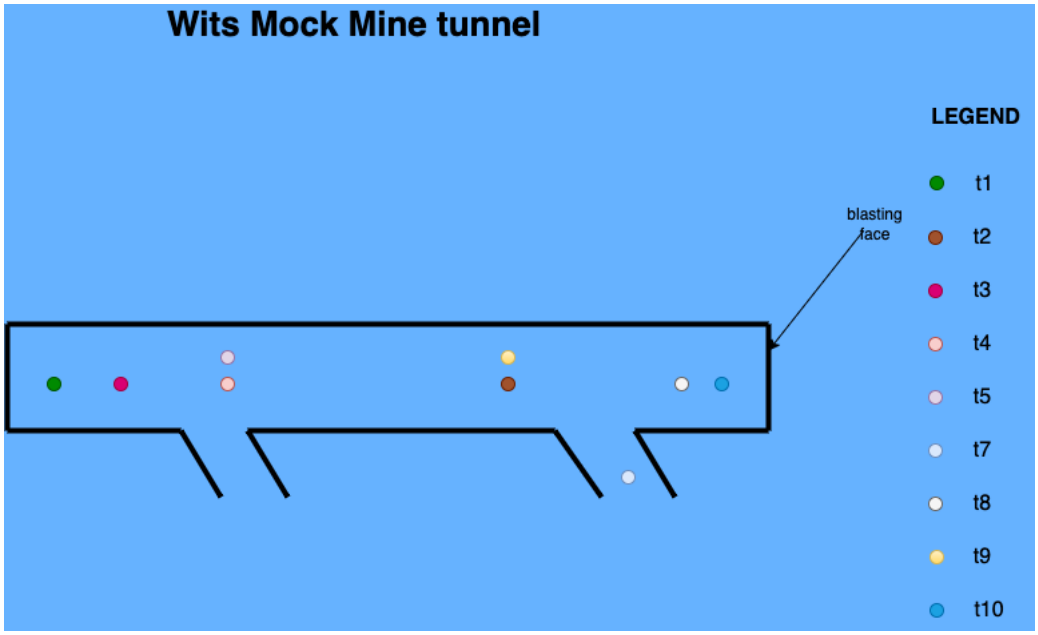


Figure 5.5: Location of survey pegs in the Wits Mock Mine tunnel used to georeference LiDAR and CRP 3D models for this research.

5.3.1 Pre-Deformation and Post-Deformation Processing of LiDAR 3D Models

Four survey pegs, namely t1, t2, t4 and t10, were used during data acquisition using LiDAR. The terrestrial laser scanner was deployed underneath t10, t2 and t4 pegs during data acquisition and data was collected between t10 and t1. The survey pegs shown in Figure 5.6 are in

the LiDAR 3D model. The backsights were t4, t2 and t1 in both the pre-deformation and post-deformation stages of LiDAR point cloud data collection.

The location of the LiDAR and its backsights is essential for optimal data alignment and registration. The LiDAR's position aids in the georeferencing of the model, while a backsight guarantees the alignment of the scanned models by enhancing consistency between scans and establishing the scans' orientation.

This method of data collection was implemented in both pre-deformation and post-deformation conditions in the Wits Mock Mine. The diversification of these survey pegs ensures a holistic 3D model of the Wits Mock Mine is reconstructed from the blasting face of the tunnel to the 20kg bags depicting rockfalls on the other side of the tunnel.

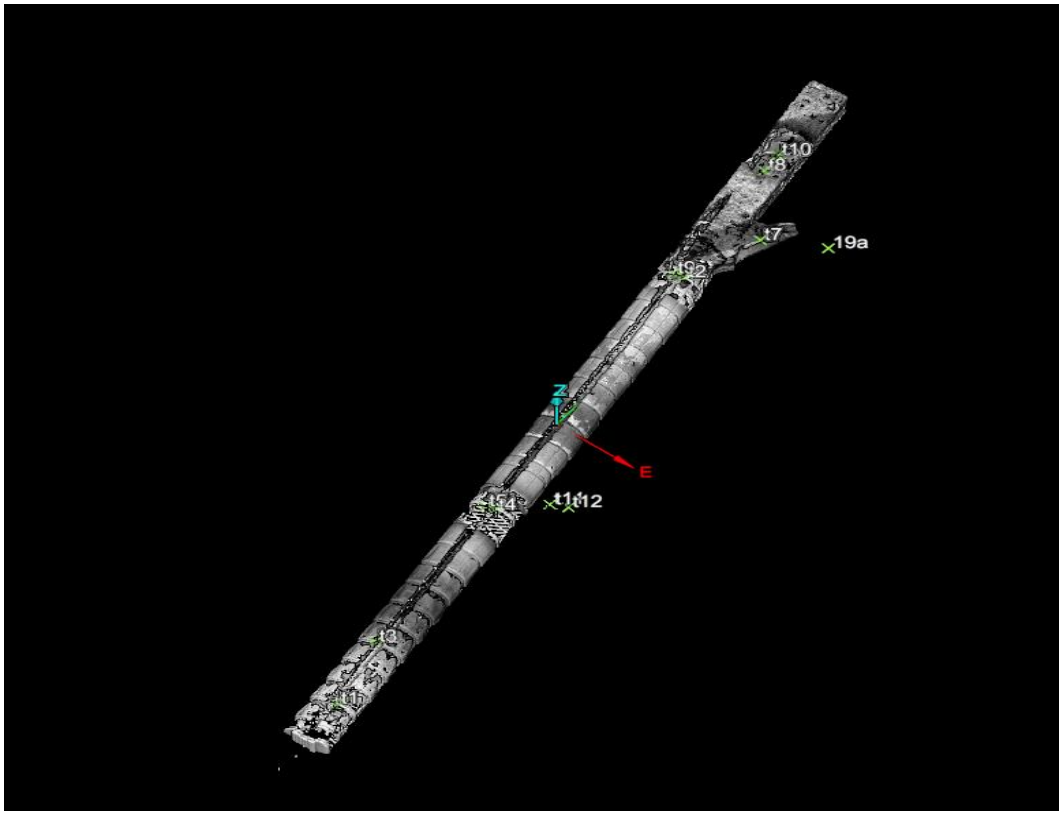


Figure 5.6: Illustration of georeferenced LiDAR point clouds with GCPs correctly positioned.

5.3.2 Pre- and Post-Deformation Processing of CRP 3D Models

In the pre-deformation stage, four survey pegs were used for analysis which are T1, T2, T5 and T7 shown in Table 5.2 obtained from MicMac software.

Table 5.2: Pegs used to georeference a CRP reconstructed 3D model in the pre-deformation stage.

Name	Easting	Northing	Altitude	Error (px)	Error (m)	# Images
T2	97219.3747	2898419.1150	1763.4144	0.6264	0.1028	4
T7	97221.1606	2898424.5632	1763.1146	0.4842	0.1475	5
T5	97221.8659	2898395.3804	1763.3015	0.7469	0.1546	4
T1	97225.2278	2898375.4264	1763.4394	0.6182	0.1014	4

Table 5.2 and Table 5.3 show the survey pegs' coordinate points.

Table 5.3: Survey pegs used to geo-reference post-deformation 3D reconstructed model with their coordinates.

Name	Easting	Northing	Altitude	Error (px)	Error (m)	# Images
T2	97219.2001	2898419.3519	1763.2329	0.8257	0.4182	6
T1	97225.1996	2898376.1423	1763.3185	0.5191	0.6261	5
T7	97220.7573	2898425.0498	1763.0351	0.9278	0.5211	5
T9	97218.3939	2898419.3173	1763.2692	0.5186	0.4851	5
T4	97222.4220	2898396.0044	1763.3649	0.5512	0.6889	5

The error is presented in both pixel and length formats. It delineates the discrepancies between the actual coordinate system and those in the reconstructed 3D model. The number of images shown in the last column were selected since they are more precise to the targeted survey pegs.

The acceptable error in pixels should be less than one as greater errors indicate more significant problems related to GCP alignment which increases inaccuracy of the reconstructed 3D model (PIX4DMapper, 2024). Errors in metres should generally not exceed 0.5 metres, particularly in research that demands more precise geometric measurements such as deformation monitoring (PIX4DMapper, 2024). Some of the errors in metres indicated in Table 5.3 are not tolerable because they are above 0.5 metres. These include T1 and T4 pegs.

These survey pegs were also strategically positioned to ensure the Wits Mock Mine tunnel was incorporated for geometric analysis. The CRP algorithms selected 2440 of 2442 images captured in the Wits Mock Mine during the pre-deformation stage.

In post-deformation, the algorithm processed 3205 images of the 3247 images captured for 3D model reconstruction. Various pegs were employed to geo-reference the reconstructed model. The survey pegs are shown in Table 5.3.

Figure 5.7 illustrates how the Wits Mock Mine model is georeferenced by uttilising survey pegs on sight. When selecting such images, it should be noted that the images are not blurry since it is difficult for SfM to identify survey pegs from such images.

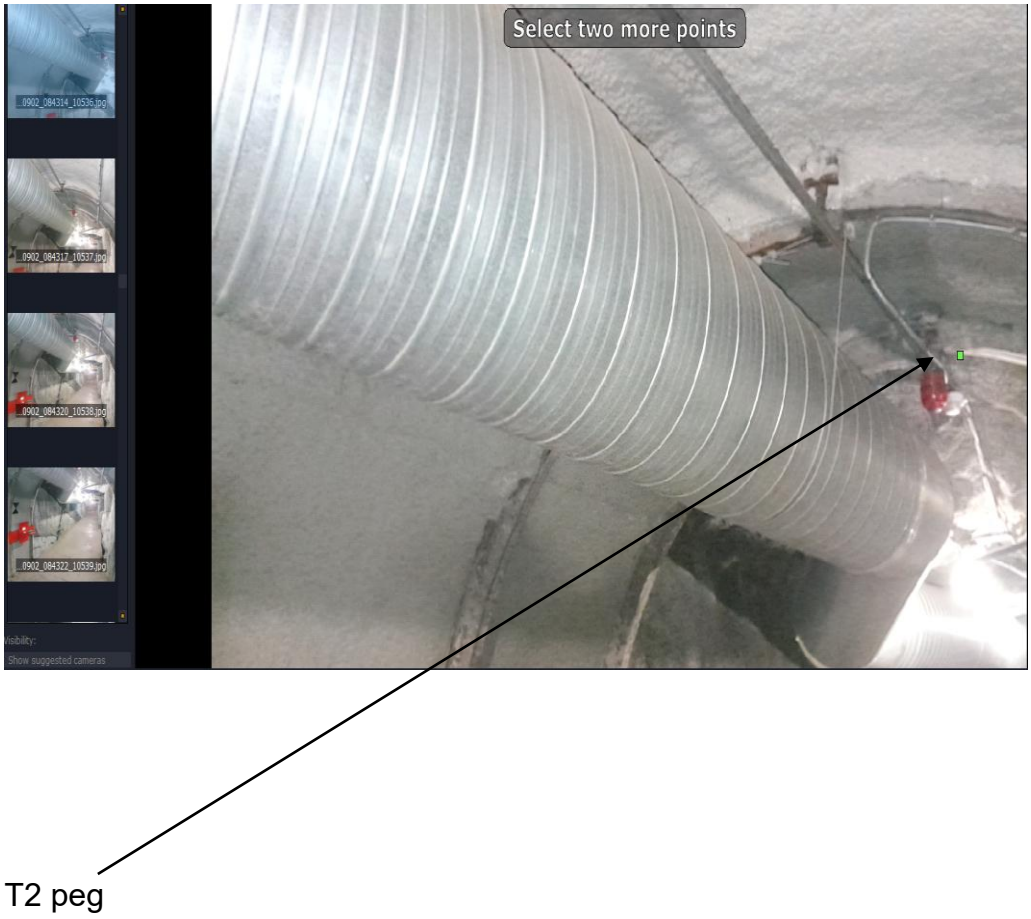


Figure 5.7: Illustration of a peg detected on an image for georeferencing of CRP 3D models.

When the survey pegs have been identified on the various images of the 3D model, the reconstructed 3D model is aligned with the constraints thus georeferencing it. Figure 5.8 shows a 3D reconstructed model with red dots indicating the GCPs that were detected. This is an indication that the reconstructed 3D model was shifted into the NCSS and measurements can be obtained and compared with true values measured.

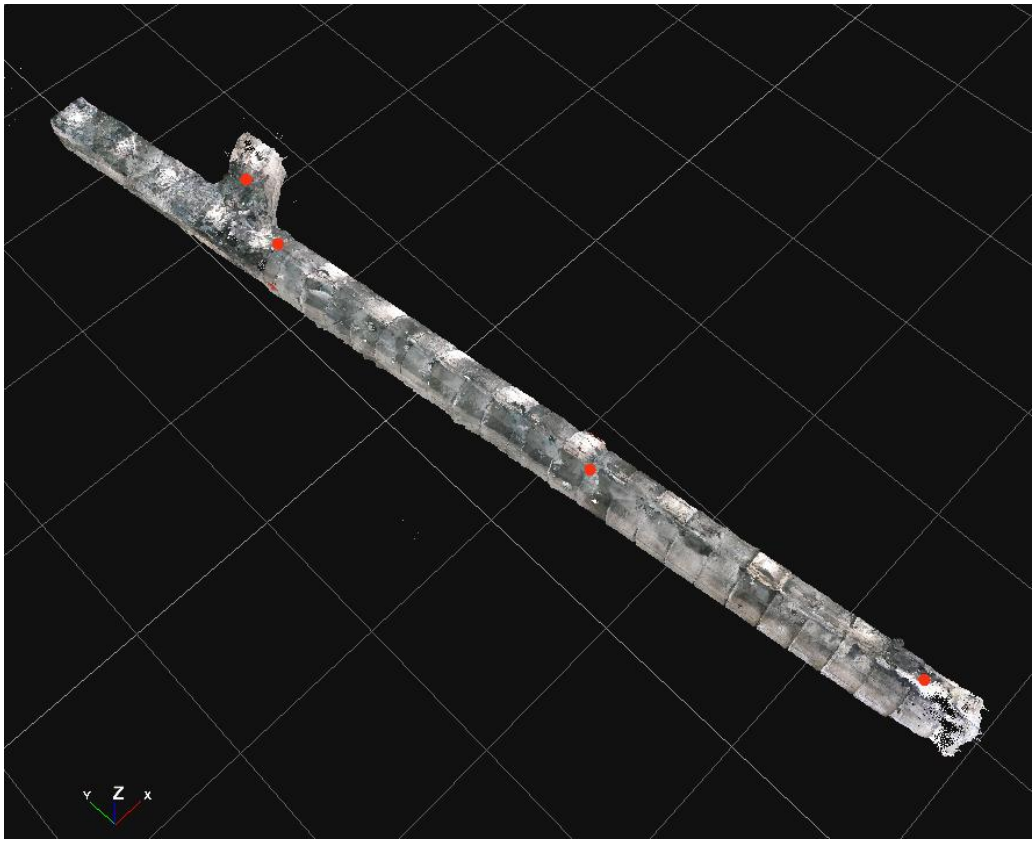


Figure 5.8: Georeferenced 3D model reconstructed using CRP principles, with GCPs incorporated within the model.

5.4 Verification of Alignment

The alignment of reconstructed 3D models is essential prior to accuracy assessment and deformation monitoring using various remote sensing technologies. Alignment was confirmed on CRP 3D models reconstructed in both pre-deformation and post-deformation stages, LiDAR 3D models reconstructed in pre-deformation and post-deformation stages and combined 3D models in both deformation states. However, after the 3D models were reconstructed, accuracy was assessed before monitoring

deformation. Deformation mapping and monitoring were executed on the preferred 3D models based on the accuracy assessment results.

5.4.1 Alignment of Fused 3D Model Dense Point Clouds in the Pre-Deformation Stage

The pre-deformation LiDAR and CRP point clouds were integrated and aligned utilising a minimum of three common ground control points (GCPs). The point clouds generated by both remote sensing technologies were unbiased, as decimation was employed to prevent overlap between the two types of point clouds. Figure 5.9 illustrates the integrated point clouds derived from LiDAR and CRP technologies during the pre-deformation phase.

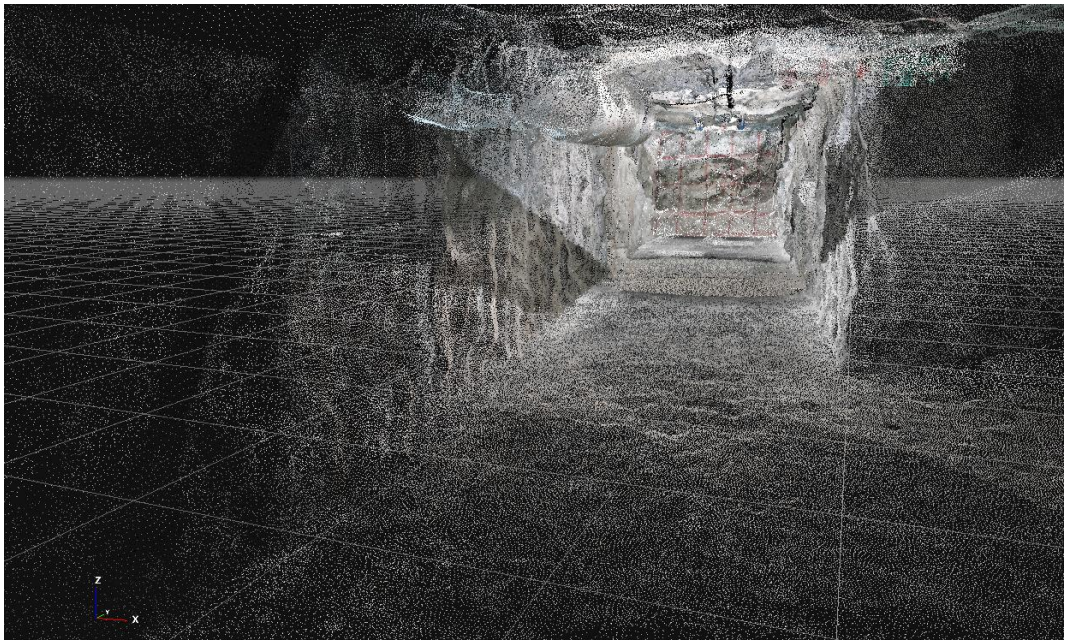
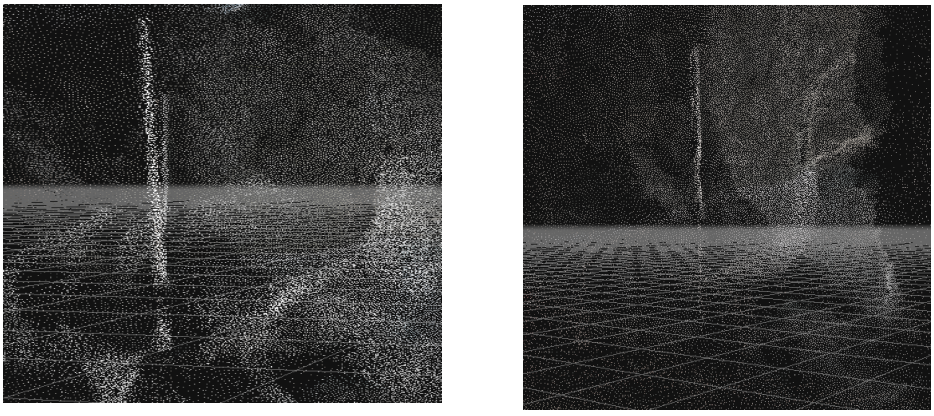


Figure 5.9: Fused 3D model from CRP and LiDAR point clouds in the pre-deformation stage.

5.4.2 Alignment of Fused 3D Model Dense Point Clouds in the Post-Deformation Stage

Integrating and aligning post-deformation point clouds from LiDAR and CRP proved difficult due to the necessity of aligning eight items within the tunnel utilising both remote sensing technologies' datasets. Following the decimation and alignment of the point clouds, the unstructured 3D model was organized, hence enhancing the correlation between LiDAR and CRP point clouds and facilitating the formation of a mesh. The objects representing deformation change were increasingly aligned, as demonstrated in Figure 5.10 with one of the objects.



a) b)

Figure 5.10: Comparison of fused LiDAR and CRP point clouds with fluorescent tube objects in a) unstructured datasets and b) structured datasets.

Accurate alignment of reconstructed 3D models is crucial because it avoids false positives resulting from alignment errors. Structuring point clouds is essential to eliminate misalignments between two different point clouds by

providing relativity between the corresponding point clouds. When the relationship between the two different point clouds has been established, a mesh can be reconstructed to quantitatively and qualitatively analyse deformation changes in the underground mining environment. Mesh generation accommodates the ability to compare the different surfaces of reconstructed 3D models, better visualisation and the ability to filter and focus on the areas of interest in the tunnel.

5.5 Textured Mesh Generation of Combined Point Clouds

To reconstruct a mesh from the combined dense point clouds, the point clouds were structured. LiDAR point clouds are not structured thus computing a mesh would not be possible. LiDAR point clouds initially exist in an unstructured format, indicating that the points are not interconnected (Shan & Toth, 2018). The structuring of LiDAR point clouds occurs post-decimation to achieve a nearly uniform point distribution with CRP point clouds, hence mitigating bias in the reconstructed 3D model from an overabundance of points from a single remote sensing technology.

Measurements derived from the generated meshes of CRP and LiDAR technologies, along with their integration, are documented in Appendices E, F, G and H. The integration of CRP and LiDAR remote sensing technologies is crucial in underground mines. The combined 3D model is photorealistic and exhibits good textural details. Figure 5.11 demonstrates the similarity between the combined reconstructed model and the primary image captured in the tunnel.



a)



b)

Figure 5:11: Comparison of textural quality of Wits Mock Mine tunnel between a) a fused 3D reconstructed model and b) an image captured using an Android device.

Alignment challenges include control point discrepancies from LiDAR and CRP technologies. The combined 3D model point clouds in pre-deformation were combined with the point clouds in post-deformation. However, an assessment was done using the ICP algorithm to ensure the combined data sets from both pre-deformation and post-deformation states were aligned. Figure 5.12 illustrates the low errors achieved in aligning the combined 3D models of pre-deformation and post-deformation before monitoring deformation using MicMac software.

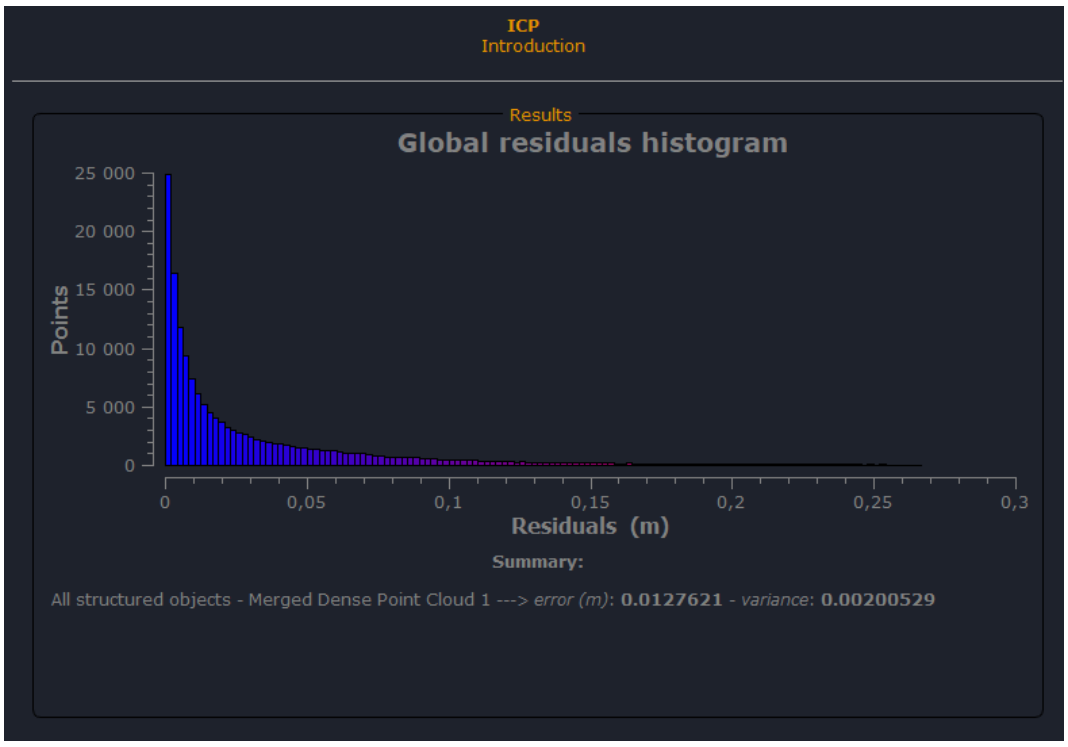


Figure 5:12: ICP global residuals graph showing the accuracy of alignment of pre-deformation and post-deformation fused point clouds.

ICP alignment is a crucial stage used to assess how the point clouds are aligned. The residuals in the x-axis show the difference in distance between two corresponding points. Therefore, the closer the corresponding points are to each other, the more aligned the 3D models. The y-axis shows the number of points within each residual value.

According to Figure 5.12, there are very low residuals because most of the points lie close to value zero on the x-axis. This indicates the points are closely aligned. As the number of residual values in the x-axis increases, the number of points significantly decreases. As indicated in Figure 5.12, the mean residual error is 12.76 millimeters and the variance is 2.00 millimeters.

The reduced mean residual error and variation, illustrated in Figure 5.12, further substantiate the accuracy of alignment. This signifies the dependability of monitoring deformation over time, as the outcomes will primarily reflect the actual changes in the underground environment rather than the misalignment of the 3D models.

When the models have been georeferenced and a mesh of the 3D models has been reconstructed, further analysis is done to assess the accuracy of the models before monitoring deformation. The assessment was conducted on the post-deformation 3D models due to the consistency in equipment and methodology used in both the pre-deformation and post-deformation stages. An accuracy assessment was also done only in the post-

deformation stage because of the primary objective of the research which is to detect changes between the pre-deformation and post-deformation stages.

5.6 Accuracy Assessment

Accuracy assessment is critical in this research to evaluate the accuracy and reliability of deformation monitoring using fused reconstructed 3D models. The precision of the integrated reconstructed 3D model was evaluated by statistical analysis, primarily utilising mean absolute error (MAE), root mean square error (RMSE), and percentage error. These indicators yield diverse insights, resulting in a more thorough evaluation of the 3D model's accuracy and performance. These metrics were selected to comprehend the discrepancies in monitoring deformation, as they encompass the magnitude and characteristics of errors.

To ascertain and validate the optimal methodology for deformation mapping and monitoring, comparisons were made among LiDAR, CRP, and combined metric data. The MAE, RMSE, and mean percentage error were computed for each item. The results were analysed, and a recommendation for the optimal model for deformation monitoring was provided. Figure 5.13 presents the measurements acquired from the eight items utilised for deformation monitoring. The three strategies were evaluated against the conventional method of data collecting. The validation of the measurements depicted in Figure 5.13 is detailed in Appendix E, Appendix F, Appendix G and Appendix H.

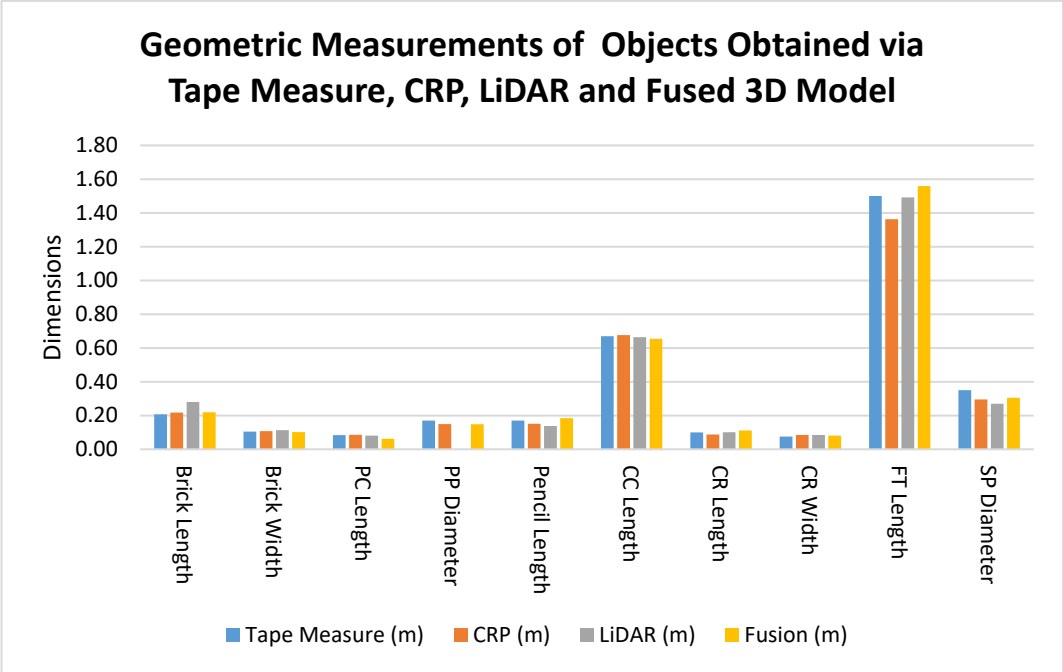


Figure 5.13: Comparison of the object dimensions obtained using a tape measure, CRP, LiDAR and fused 3D model.

Abbreviations: PC (plastic cup), PP (plastic plate), CC (cylindrical container), CR (concrete rock), FT (fluorescent tube), SP (spherical paper)

One dimension of the plastic plate could not be detected by LiDAR, resulting in its exclusion from the error calculation.

5.6.1 Mean Absolute Error

The mean absolute error was employed for accuracy assessment as it quantifies the amount of errors irrespective of their direction. This facilitates the interpretation of the proximity between the assessed value and the observed values. Significant errors are integrated similarly to minor errors,

in contrast to other metrics such as RMSE, where errors are squared. Consequently, the significant errors identified as outliers have reduced sensitivity (Chai & Draxler, 2014).

Equation (5.1) shows the formula used to calculate LiDAR measurements MAE in contrast to observed values with a tape measure.

$$\textit{LiDAR MAE} = \frac{1}{n}\sum_{i=1}^{n} \quad |LiDAR\ Measurement_i - Tape\ Measurement_i| \tag{5.1}$$

LiDAR MAE = 0.025 m

Equation (5.2) provides the formula for how MAE was obtained between CRP and tape measure results.

$$\textit{CRP MAE} = \frac{1}{n}\sum_{i=1}^{n} \quad |CRP\ Measurement_i - Tape\ Measurement_i| \tag{5.2}$$

CRP MAE = 0.028 m

The MAE between measurements from a combined reconstructed model and tape measure values was calculated using the formula:

$$\textit{Fused model MAE} = \frac{1}{n}\sum_{i=1}^{n} \quad |Fused\ Measurement_i - Tape\ Measurement_i|. \tag{5.3}$$

Fused model MAE = 0.021 m

5.6.2 Root Mean Square Error (RMSE)

RMSE is essential to assess the accuracy of reconstructed 3D models because it includes larger errors that have a significant effect on the

outcome. This provides more detail including the most undesirable results. Assessing the accuracy using both MAE and RMSE provides more insights regarding the reconstructed 3D models. Equation (5.4) shows how LiDAR RMSE was calculated (Willmott & Matsuura, 2005).

$$\textit{LiDAR RMSE} = \sqrt{\frac{1}{n}\sum_{i=1}^{n} \quad (LiDAR\ Measurement_i - Tape\ Measurement_i)^2} \tag{5.4}$$

LiDAR RMSE = 0.038 m

Equation (5.5) indicates how CRP RMSE was calculated, it's RMSE is slightly larger than LiDAR RMSE.

$$\textit{CRP RMSE} = \sqrt{\frac{1}{n}\sum_{i=1}^{n} \quad (CRP\ Measurement_i - Tape\ Measurement_i)^2} \tag{5.5}$$

CRP RMSE = 0.048 m

RMSE of the combined 3D model was calculated as shown in equation (5.6).

$$\textit{Fused model RMSE} = \sqrt{\frac{1}{n}\sum_{i=1}^{n} \quad (Fused\ Measurement_i - Tape\ Measurement_i)^2} \tag{5.6}$$

Fused model RMSE = 0.027 m

5.6.3 Percentage Error

The Percentage Error relates the calculated error of the model with the observed data. The error difference is compared in percentage format not only between models being assessed but also between the model and the true value.

Equations (5.7) and (5.8) illustrate how percentage error was calculated on both LiDAR and CRP models respectively.

$$\textit{LiDAR Percentage Error} = \frac{|LiDAR\ Measurement - Tape\ Measurement|}{Tape\ Measurement} \textit{ x 100.} \quad (5.7)$$

LiDAR Percentage Error = 11.54%

$$\textit{CRP Percentage Error} = \frac{|CRP\ Measurement - Tape\ Measurement|}{Tape\ Measurement} \textit{ x 100} \quad (5.8)$$

CRP Percentage Error = 8.43%

$$\textit{Fused Percentage Error} = \frac{|Fused\ Measurement - Tape\ Measurement|}{Tape\ Measurement} \textit{ x 100} \quad (5.9)$$

Fused Percentage Error = 9.33%

5.6.4 Comparison and analysis of accuracy assessment metrics

Table 5.4 shows the summary of the accuracy assessment metrics, MAE, RMSE each remote sensing technology and its fusion. MAE and RMSE are provided in units of the measurements provided, in this case, in metres.

Table 5.4: Summary of the calculated errors of CRP, LiDAR and fused 3D model metrics with observed measurements from the tape measure.

	CRP	**LiDAR**	**Fusion**
MAE	0.0276m	0.0246m	0.0209m
RMSE	0.0481m	0.0380m	0.0268m
Mean % Error	8.43%	11.54%	9.33%
Difference from fusion	-0.9%	2.21%	

Mean percentage error provides the percentage difference between the calculated metric with the absolute value.

The combined 3D model measurements exhibit lower MAE and RMSE in comparison to CRP and LiDAR metrics. This is a significant indicator that a fused 3D model can be utilised to monitor deformation. CRP has the lowest mean percentage error whereas the fused 3D model has a slightly more percentage error of 0.90% compared to CRP and is 2.21% less than LiDAR. According to these results, a 3D model reconstructed from the fusion of CRP and LiDAR point clouds is crucial for deformation monitoring because of the reliability it has gained from its accuracy assessment.

5.7 Deformation Mapping and Monitoring

5.7.1 Point-to-Point Comparison

A point-to-point comparison was made between the pre-deformation and post-deformation of combined 3D models. This is comparing the individual points from the two corresponding 3D models. The histogram in Figure 5.14 analyses any slight changes with colour indicating the points' variations; this concept is known as distance residuals.

The x-axis of the histogram in Figure 5.14 shows the magnitude of the distance residuals between points. The magnitude of the distance residuals increases from blue to red.

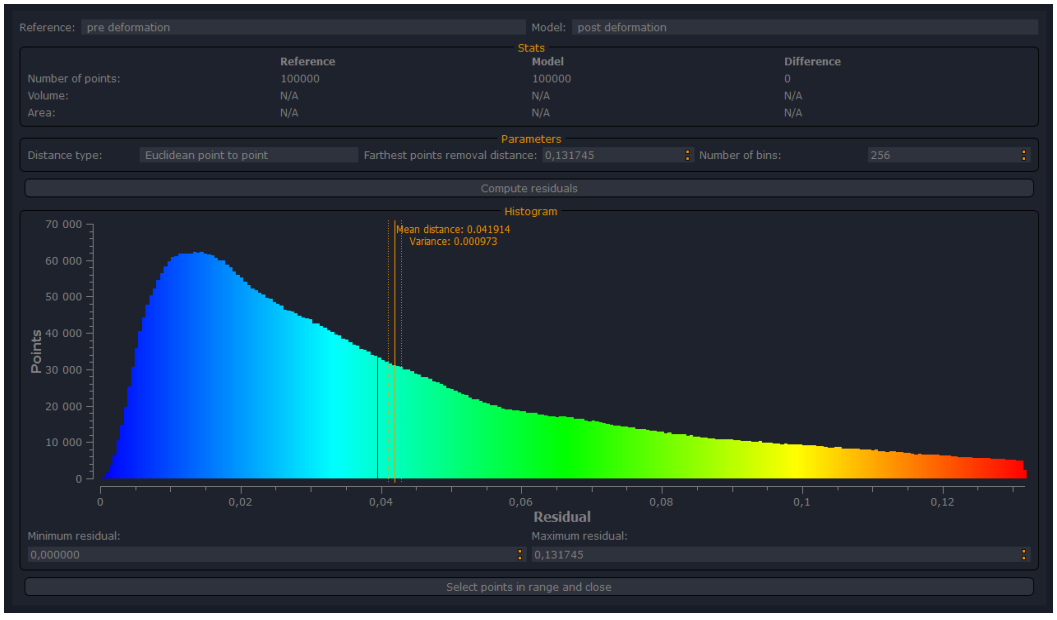


Figure 5.14: Residual histogram indicating differences in points between pre-deformation and post-deformation.

Colours from blue to green show minimal residuals meaning there is very small or no movement at all with values of distance residual ranging between 0 to 0.085m. Colours from yellow to red indicate higher distance residuals between points indicating there are larger deformations or movement. Therefore, the deviation of points increases from the left to the right of the x-axis of the histogram.

The y-axis of the histogram in Figure 5.14 indicates the number of points corresponding to the distance residuals. Most of the points of the 3D model in the blue zone indicate there was good alignment of points between the pre-deformation and the post-deformation stages did not change. This aligns well with the test since only a few objects are placed in the tunnel compared to the whole area of the tunnel. However, as the residuals decreased, there were major deviations between points.

5.7.2 Heat Map

A heat map is one of the many ways to map and monitor deformation. In this research, a heat map was used to indicate subtle changes in the Wits Mock Mine tunnel between the pre-deformation and post-deformation 3D models. However, some of the changes might have come from the misalignment between the pre-deformation and post-deformation 3D models, which would have had subtle changes when combining LiDAR and CRP point clouds. However, the intensity of detecting minor deformation changes in underground mines can improve accuracy thus deploying necessary steps for risk mitigation and safety in underground mines.

Figure 5.15 shows a heat map of the Wits Mock Mine tunnel. The Wits Mock Mine tunnel indicated in Figure 5.15 is a post-deformation 3D model which uses a pre-deformation 3D model as its reference for changes. The heat map has different colour codes that illustrate changes in a particular location of the Wits Mock Mine. The different colour codes are illustrated using a histogram in Figure 5.16. Table 5.5 indicates five objects that were detected showing measurable movement thus aligning with the research's objectives.

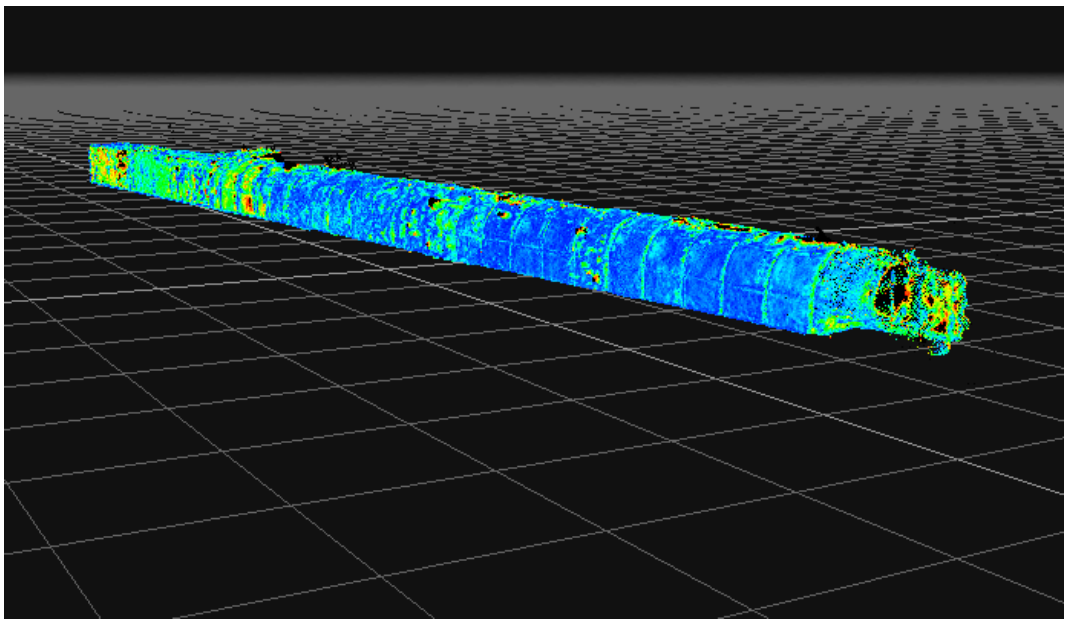


Figure 5.15: A post-deformation 3D model heat map of the Wits Mock Mine tunnel.

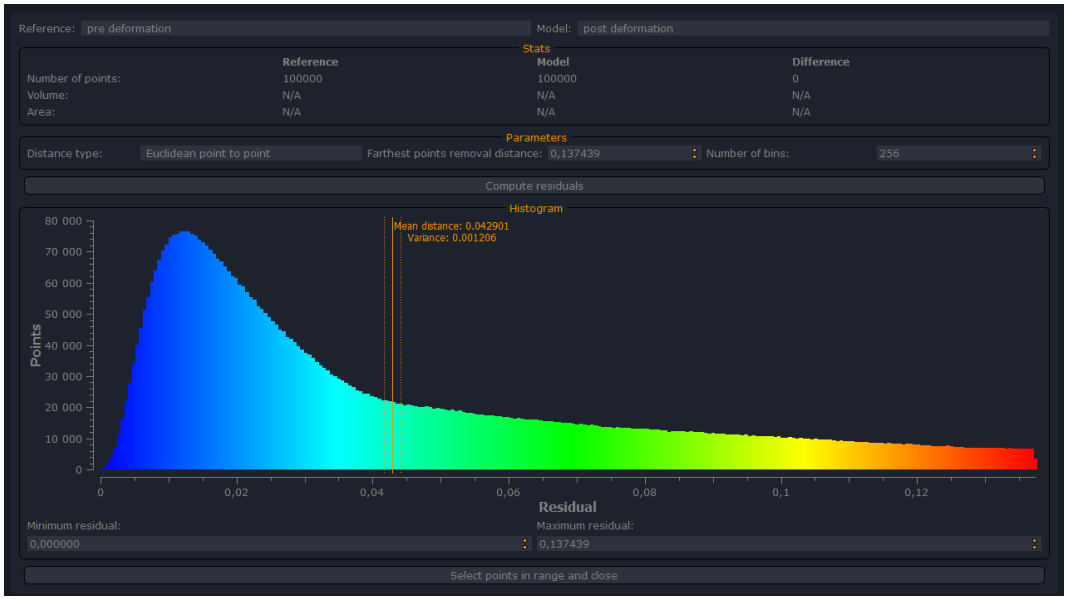
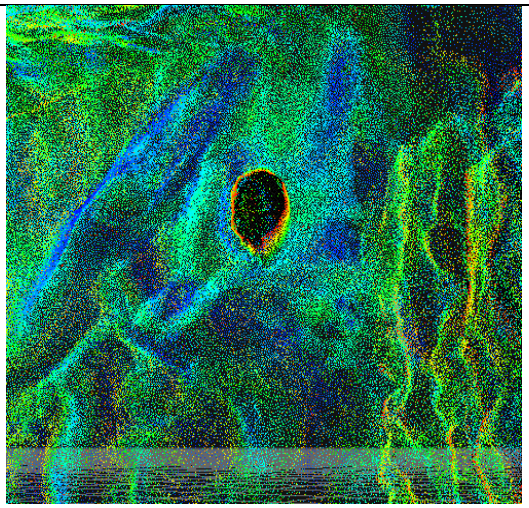
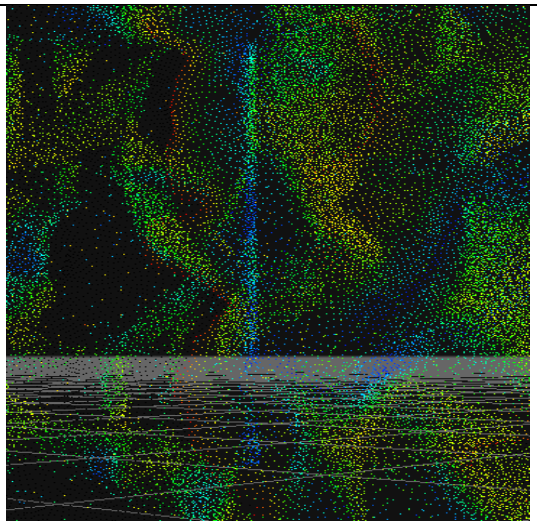
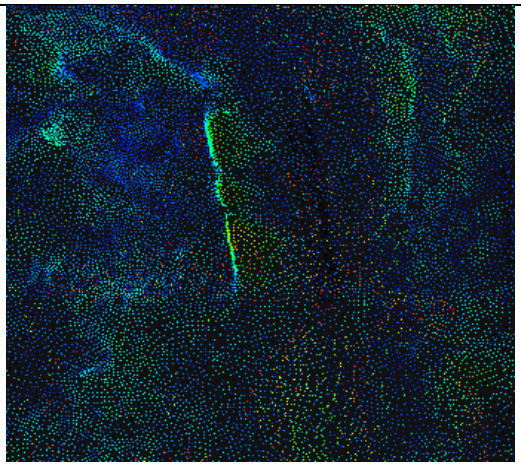
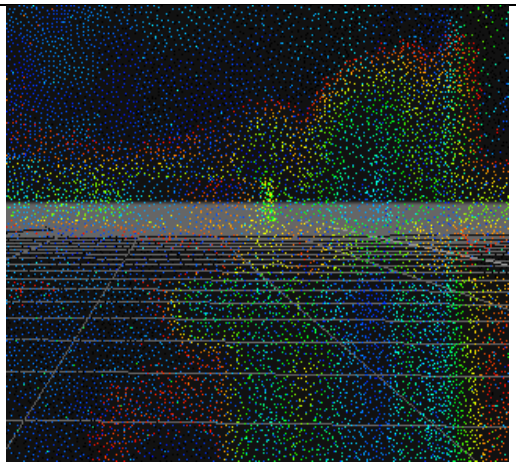
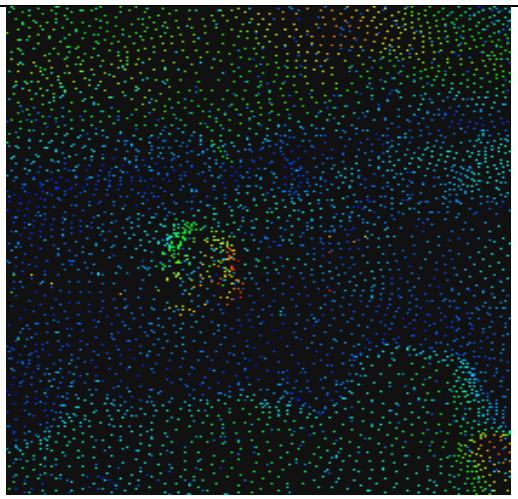


Figure 5.16: A histogram illustrating the relationship between the number of points in the post-deformation 3D model with its residual.

Table 5.5: Heat map of objects placed in the Wits Mock Mine tunnel representing deformation.

Name of object	Heat map of the object
1. Spherical paper	

2. Fluorescent tube	
3. Cylindrical container	
4. Brick	

5. Plastic cup	

a) Spherical paper

The colour changes from blue, which indicates minimal displacement, to red on the edges of the object illustrating significant displacement in those areas. This indicates a spherical block can be detected due to the changes in the surrounding zones. The changes in colour gradient show the concentration of stress surrounding the object. Monitoring blocks of the same structure can provide early warnings of any structural changes that might lead to FOGs.

b) Fluorescent tube

The object represents vertical line of deformation, with varying colour changes along the vertical axis; this shows vertical separations in the tunnel wall. Tracking vertical deformations is necessary to monitor cracks over time especially in underground mines.

c) Cylindrical container

A green-yellow colour pattern signifies a narrow deformation zone. Small deformation changes indicate small fractures and are useful in monitoring the stability of tunnel surfaces. Such deformations can expand resulting in significant hazardous issues if not addressed early.

d) Brick

The object has a mixed colour pattern illustrating the scattered deformation across the surface. The changes suggest an ongoing subsidence. Continuous monitoring of the object in this zone detects the changes in movement which can impact the overall safety of the mine.

e) Plastic cup

The colour variation on the object is separated from the rest, with a concentrated colour pattern. This is essential as isolated anomalies are crucial to monitor because they can indicate hidden stress points that are not yet apparent. Monitoring such zones facilitates the early identification of possible risks prior to their escalation into significant structural problems.

5.8 Chapter Summary

Chapter 5 focused on the pipeline from data acquisition using a tape measure, LiDAR, CRP and fused data sets of LiDAR and CRP to the comparison of their geometric measurements. A tape measure was used to measure all the eight objects' dimensions which is the conventional method

used in this research. LiDAR, CRP and fusion of the two remote sensing technologies were also used with identified better workflows to obtain their best outcomes of 3D reconstructed models.

Pre-deformation and post-deformation stages in this research are defined by placing the eight objects in the Wits Mock Mine. Pre-deformation stage in this scenario is when there are no objects placed in the Wits Mock Mine whereas in the post-deformation stage, all eight objects are placed. These eight objects have varying sizes and structures to depict different deformation magnitudes that occur underground, with varying positioning of deformation put into account.

Parameters that occur in the underground mine were incorporated in this chapter. Some of the parameters include the positions where deformation is most likely to occur and lighting conditions. Therefore, the remote sensing technologies were implemented in the Wits Mock Mine tunnel whilst the underground mine conditions were optimised.

LiDAR and CRP reconstructed 3D models were registered before georeferencing them. Three LiDAR point cloud scans were registered and aligned under a fixed reference system which was the baseline for LiDAR pre-deformation and post-deformation comparisons. CRP uses SIFT, image matching algorithm, bundle, adjustment, camera calibration and structure from motion. The remote sensing technologies' point clouds were fused before generating a textured mesh.

The study's findings demonstrated that the fused 3D model achieved higher image quality than the standalone LiDAR model and reduced both the mean absolute error (MAE) and root mean square error (RMSE). The fusion successfully captured and monitored deformation within the Wits Mock Mine tunnel, detecting subtle changes with a mean residual of 41.914 millimeters. This capability provides mining professionals with critical early warning signs of instability, enabling them to implement timely safety measures to prevent dangerous rockfalls that could threaten both personnel and equipment.

6 CONCLUSIONS, LIMITATIONS AND RECOMMENDATIONS

The application of remote sensing technologies in underground mining is vital for enhancing both safety and operational efficiency. Underground mines are inherently hazardous environments, presenting risks such as FOGs, toxic gases, fires, and explosions, all of which require continuous monitoring. Remote sensing technologies are primarily used to track and map ground deformation, a crucial factor in maintaining underground safety. However, challenges remain regarding the extent to which these technologies can deliver accurate data under adverse conditions, including dust, humidity, low light, and limited access.

6.1 Conclusions

Qualitative and quantitative analyses were conducted on three models: the LiDAR model, the CRP model, and a fused 3D model. The results indicated that the fused model offered improved accuracy and enhanced spatial representation by combining the strengths of both technologies. CRP, which uses a passive sensor, and LiDAR, which employs an active sensor, complement each other. Their integration resulted in a more comprehensive model that addressed the limitations of each standalone technology.

This dissertation demonstrates the potential of integrating CRP and LiDAR for accurate and reliable deformation monitoring in underground mines. By combining the geometric precision of LiDAR with the high-resolution texture

detail of CRP, the fused datasets provide enhanced spatial completeness, improved deformation detection and richer contextual information than either technique alone.

6.2 Recommendations

However, several challenges were encountered during the research. Outliers in the data significantly affected the precision of deformation monitoring, skewing results. Additionally, the textured mesh of the fused model contained noise, requiring post-processing to improve accuracy. To address these issues, the following recommendations were proposed:

- Integration of LiDAR and CRP Sensors:

  Developing a single device that combines both active (LiDAR) and passive (CRP) sensors could streamline data collection and reduce data gaps, especially in environments with poor lighting and complex geometries.

- Annual Calibration of Laser Scanners:

  The laser scanner used in this study had not been calibrated for several years, potentially affecting measurement accuracy. Regular annual calibration is recommended to maintain data precision.

- Optimized Equipment for Data Collection:

  Utilizing a LiDAR scanner with a shorter range can offer a cost-effective solution for underground mining applications. Additionally, employing a

camera with higher image quality can enhance registration accuracy and improve the overall performance of fused 3D models.

These recommendations emphasize the need for continuous equipment maintenance, technological advancement, and methodological refinement to enhance the performance of remote sensing technologies in underground mining. The findings underscore that a well-integrated 3D model, which capitalizes on the complementary capabilities of CRP and LiDAR, is crucial for accurate deformation monitoring and improved safety management in underground mining operations.

6.3 Limitation of Study and Future Research Work

One significant obstacle is the absence of Global Positioning System (GPS) signals in underground settings. Many remote sensing systems rely on GPS for precise data acquisition. This study addressed this limitation by employing GCPs. In the Wits Mock Mine, pegs with known coordinates were used to georeference both CRP and LiDAR models.

CRP models were constructed by capturing images of these reference points, while LiDAR models were aligned by positioning the scanner directly beneath the pegs and using a backsight for calibration. The integration of the two models was achieved using MicMac software, which aligned the data on a unified platform.

Humidity, lighting conditions and dust in underground mines affect the accuracy of 3D model reconstruction. CRP depends on good lighting conditions to obtain quality images which are used to reconstruct 3D models. Dust and humidity may hinder adequate acquisition of desired scans of the mine.

Regarding future work, there should be improved sensor integration. Developing a hybrid LiDAR and camera rigs with synchronised data capture to minimise temporal misalignment of 3D models. In terms of low-light environments, multispectral or hyperspectral imaging can be used alongside RGB to improve texture matching.

Other illumination strategies such as uniform lighting systems specifically optimised for photogrammetric imaging in underground settings can be done. Other active imaging technologies such as structured light and flash LiDAR can be used to overcome poor ambient lighting.

Noise removal and co-registration of data should be automated. One of the best possible ways is implementation of AI-based algorithms for automated point cloud registration between LiDAR and CRP datasets. Deep learning can be used for dust and noise filtering to improve measurement reliability.

Real-time monitoring capabilities can be further improved by mounting fused LiDAR and CRP technologies on mobile platforms such as autonomous ground robots or UAVs adapted for confined spaces. On-site

processing pipelines can be used to enable near-real-time deformation patterns.

7 REFERENCES

Abellán, A., Calvet, J., Vilaplana, J. M. & Blanchard, J., 2010. Detection and spatial prediction of rockfalls by means of terrestrial laser scanner monitoring. 119(3), pp. 162-171.

Ahmad, N., Ghazilla, R. A. R., Khairi, N. M. & Kasi, V., 2013. Reviews on Various Inertial Measurement Unit (IMU) Sensor Applications. *International Journal of Signal Processing Systems,* pp. 256-262.

Altuntas, C., 2021. Triangulation and time-of-flight based 3D digitalisation techniques of cultural heritage structures. *The International Archives of the Photogrammetry, Remote Sensing and Spatial Information Sciences*, pp. 825-830.

Ashraf, M. A., Mahmood, A. & Mahboob, M. A., 2022. Numerical evaluation of specific absorption rate in human head and torso for wearable wireless devices in underground mine scenarios. *Radiation Protection Dosimetry,* 198(8), pp. 491-502.

Basahel, H. & Mitri, H., 2017. Application of rock mass classification systems to rock slope stability assessment: A case study. *Journal of Rock Mechanics and Geotechnical Engineering,* 9(6), pp. 993-1009.

Bazzi, H., Noferesti, H. & Farhadian, H., 2020. Modelling the effect of blast-induced vibrations on the stability of a faulted mine slope. *Journal of the Southern African Institute of Mining and Metallurgy,* 120(10), pp. 591-597.

Benton, D. J., Chambers, A. J., Raffaldi, M. J., Finley, S. J., Powers, M. J., 2016. Close-range photogrammetry in underground mining ground control. San Diego, California, United States, p. 997707.

Berberan, A., Marcelino, J., Boavida, J. & Oliveira, A., 2007. Deformation monitoring of earth dams using laser scanners and digital imagery., Alan Manchester; Contribiting Editor; Hydropower & Dams.

Chikande, T. & Zvarivadza, T., 2016. Review of support systems used in poor ground conditions in platinum room and pillar mining: A Zimbabwean case study. *Journal of the Southern African Institute of Mining and Metallurgy,* 116(4), pp. 323-332.

Costantino, D., Pepe, M. & Alfio, V., 2020. Point Cloud accuracy of Smartphone Images: Applications in Cultural Heritage Environment. *International Journal of Advanced Trends in Computer Science and Engineering,* Volume 9, pp. 6259-6767.

Ding, Q., Wang, F., Chen, J., Wang, M., Zhang., 2022. Research on Generalized RQD of Rock Mass Based on 3D Slope Model Established by Digital Close-Range Photogrammetry. 14(9), p. 2275.

Feroze, T. & Genc, B.,.2017. Analysis of the effect of ducted fan system variables on ventilation in an empty heading using CFD. *J. S. Afr. Inst. Min. Metall.* [online], pp.157-167.

Forkuo, E. K., 2005. Automatic Fusion Of Photogrammetric Imagery And Laser Scanner Point Clouds*,* Hong Kong.

Fraser, C. S. & Brown, D. C., 1986. Industrial Photogrammetry: New Developments And Recent Applications. *Wiley Online Library*, October, 12(68), pp. 197-217.

Gašparović, M. & Malarić, I., 2012. Increase of readability and accuracy of 3D models using fusion of close range photogrammetry and laser scanning. *The International Archives of the Photogrammetry, Remote Sensing and Spatial Information Sciences,* pp. 93-98.

Grussenmeyer, P., Alby, E., Landes, T., Koehl, M., Guillemin, S., Hullo, 2012. Recording Approach of Heritage Sites Based on Merging Point Clouds from High Resolution Photogrammetry and Terrestrial Laser Scanning. *ISPRS International Archives of the Photogrammetry, Remote Sensing and Spatial Information Sciences.*

Haala, N. & Alshawabkeh, Y., 2006. Combining Laser Scanning and Photogrammetry-A Hybrid Approach for Heritage Documentation*,* Stuttgart.

Hartley, R. & Zisserman, A., 2003. Multiple view geometry in computer vision*,* Cambridge University Press.

He, M. & Wang, Q., 2023. Rock dynamics in deep mining. *International Journal of Mining Science and Technology,* 33(9), pp. 1065-1082.

Holst, C., Neuner, H., Wieser, A., Wunderlich, T., Kuhlmann, H., 2016. Calibration of Terrestrial Laser Scanners. *Allgemeine Vermessungs-Nachrichten: AVN; Zeitschrift für alle Bereiche der Geodäsie und Geoinformation,* 123.2016(6), pp. 147-157.

Hong, G. & Zhang, Y., 2007. Combination of Feature-based and Area-based Image Registration Technique for High Resolution Remote Sensing Image. *IEEE International Geoscience and Remote Sensing Symposium,* pp. 377-380.

Jansa, J., Studnicka, N., Forket, G., Haring, A., Kager, H., 2004. Terrestrial laserscanning and photogrammetry – acquisition techniques complementing one another.

Jiang, N., Li, H., Li, C., Xiao, H., Zhou, J., 2022. A Fusion Method Using Terrestrial Laser Scanning and Unmanned Aerial Vehicle Photogrammetry for Landslide Deformation Monitoring Under Complex Terrain Conditions. *IEEE Transactions on Geoscience and Remote Sensing,* pp. 1-14.

Karami, E., Prasad, S. & Shehata, M., 2017. Image Matching Using SIFT, SURF, BRIEF and ORB: Performance Comparison for Distorted Images.

Kolapo, P., 2019. Towards a Short-Range Laboratory for Testing the Accuracy of Terrestrial 3D Laser Scanning (TLS) Technologies*,* University of Witwatersrand: MSc dissertation.

Lato, J. M. & Voge, M., 2012. Automated mapping of rock discontinuities in 3D lidar and photogrammetry models. *International Journal of Rock Mechanics & Mining Sciences,* pp. 151-157.

Lawton, G., 2022. Data preprocessing. *TechTarget*, January.

Li, G., Cao, S., Luo, F., Li, Y., Wei, Y.., 2018. Research on mining-induced deformation and stress, insights from physical modeling and theoretical analysis. *Arabian Journal of Geosciences,* 11(5), p. 100.

Lerma, J. L., Navarro, S., Cabrelles, M. & Villaverde, V., 2010. Terrestrial laser scanning and close range photogrammetry for 3D archaeological documentation: the Upper Palaeolithic Cave of Parpalló as a case study. *Journal of Archaeological Science,* 37(3), pp. 499-507.

Luhmann, T., Chizhova, M. & Gorkovchuk, D., 2020. Fusion of UAV and Terrestrial Photogrammetry with Laser Scanning for 3D Reconstruction of Historic Churches in Georgia. 4(3).

Mahmood, A., Ashraf, M. A. & Musa, G. C. F. T., 2024. An analysis of wireless signal propagation in collapsed mine scenarios. *Physical Communication,* Volume 62, p. 102250.

Ma, L., Liu, Y., Zhang, X., Ye, Y., Yin, G. & Johnson, B. A., 2019. Deep learning in remote sensing applications: A meta-analysis and review. *ISPRS Journal of Photogrammetry and Remote Sensing,* Volume 152, pp. 166-177.

Nocerino, E., Menna, F. & Verhoeven, G. J., 2022. Good vibrations? How image stabilisation influences photogrammetry. *The International Archives of the Photogrammetry, Remote Sensing and Spatial Information Sciences,* Volume XLVI-2-W1-2022, pp. 395-400.

Paar, G., Bauer, A. & Kontrus, H., 2005. Texture-Based Fusion between Laser Scanner and Camera for Tunnel Surface Documentation.

Papachristos, C., Khattak, S., Mascarich, F. & Alexis, K., 2019. Autonomous Navigation and Mapping in Underground Mines Using Aerial Robots. Big Sky, MT, USA, pp. 1-8.

Peltoketo, V.-T., 2015. Mobile phone camera benchmarking in low light environment.

Pfeifer, N., Dorninger, P., Haring, A. & Fan, H., 2007. Investigating terrestrial laser scanning intensity data: quality and functional relations. *8th Conference on Optical 3-D Measurement Techniques.*

PIX4DMapper, 2024. High georeferencing errors in the quality report. [Online]
Available at: https://support.pix4d.com/hc/en-us/articles/8965072104221?
[Accessed 25 January 2025].

Raval, S., Banerjee, B. P., Kumar Singh, S. & Canbulat, I., 2019. A Preliminary Investigation of Mobile Mapping Technology for Underground Mining. Yokohama, Japan.

Rönnholm, P., Honkavaara, E., Litkey, P., Hyyppä, H. & Hyyppä, J., 2007. Integration of laser scanning and photogrammetry. p. 9.

Sadeghi, S., Soltanmohammadlou, N. & Nasirzadeh, F., 2022. Applications of wireless sensor networks to improve occupational safety and health in underground mines. *Journal of Safety Research,* pp. 8-25.

Santise, M., Thoeni, K., Roncella, R. D. F. & Giacomini, A., 2018. Analysis of low-light and night-time stereo-pair images for photogrammetric reconstruction. *The International Archives of the Photogrammetry, Remote Sensing and Spatial Information Sciences,* Volume XLII-2, pp. 1015-1022.

Sasaoka, T., 2016. Effect of Mine Water on the Stability of Underground Coal Mine Roadways. *Geotech Geol Eng,* 34(2), pp. 671-678.

Schindler, K., 2015. Mathematical foundations of photogrammetry. In: *Handbook of Geomathematics.* Berlin, Heidelberg: Springer, pp. 3087-3103.

Shan, J., & Toth, C. K. (Eds.). (2018). Topographic Laser Ranging and Scanning: Principles and Processing (2nd ed.). CRC Press.

Singh, S., Banerjee Pratap, B. & Raval, S., 2023. A review of laser scanning for geological and geotechnical applications in underground mining. *International Journal of Mining Science and Technology,* 33(2), pp. 113-154.

Slaker, B., 2015. Monitoring Underground Mine Displacement Using Photogrammetry and Laser Scanning.

Slaker, B. A. & Mohamed, K. M., 2017. A practical application of photogrammetry to performing rib characterization measurements in an

underground coal mine using a DSLR camera. *International Journal of Mining Science and Technology,* 27(1), pp. 83-90.

Taufik, M. & Puspitasari, V. P., 2019. Geometric accuracy analysis of the measurement Ground Control Point (GCP) in the rectification process of high resolution satellite image with polynomial method (case study: Wlingi Sub-district, Blitar Regency). *IOP Conference Series: Earth and Environmental Science,* 389(1), p. 012040.

Van der Merwe, J. & Andersen, D., 2013. Applications and benefits of 3D laser scanning for the mining industry. *Journal of the Southern African Institute of Mining and Metallurgy*.

Verykokou, S. & Ioannidis, C., 2018. A photogrammetry-based structure from motion algorithm using robust iterative bundle adjustment techniques. *ISPRS Annals of the Photogrammetry, Remote Sensing and Spatial Information Sciences,* pp. 73-80.

Vorster, B. & Frankin, D., 2008. Immediate ground support, after development or stope face exposure, can prevent falls of ground. *Proceedings of Narrow Vein and Reef.*

Wang, M., Zhou, J., Shi, A., Han, J & Li, H., 2020. Key Factors Affecting the Deformation and Failure of Surrounding Rock Masses in Large-Scale Underground Powerhouses. *Advances in Civil Engineering,* 2020(1), p. 8843466.

Westoby, M., Brasington, J., Glasser, N., Hambrey, M., & Reynolds, J. (2012). ‘Structure-from-Motion’ photogrammetry: A low-cost, effective tool for geoscience applications. *Geomorphology, 179*, 300–314.

Wu, B. & Tang, S., 2015. Review of geometric fusion of remote sensing imagery and laser scanning data. *International journal of image and data fusion,* 6(2), pp. 97-114.

Wu, X., Guo, Q., Li, P., Ren, F, Zhang, J & Cai, M., 2021. Investigating the Effect of Temperature Changes on the Physical Field of Surrounding Rock in a Deep Gold Mine. *Advances in Materials Science and Engineering,* 2021(1), p. 8490864.

Zaman, I., Förster, A. & Cawood, F., 2018. Finding Trapped Miners with Wireless Sensor Networks*,* p. 1-8.

Zhang, L., Chen, Z., Bao, M., Nian, G., Zhou, Z & Zhu, T., 2022. Stability analysis and movement process determination of rock masses under open-pit to underground mining conditions. *Geomechanics and Geophysics for Geo-Energy and Geo-Resources,* 8(5), p. 148.

Zhang, X., Qi, Y., Xu, J., Du, X., Lai, J., Tan, W. & Huang, P., 2020. Application of Multi-data Fusion Technology in Landslide Monitoring. *IOP Conf. Series: Earth and Environmental Science*.

Appendix A LiDAR Data Acquisition in the Wits Mock Mine During the Pre-Deformation Stage.

1. **First Control Point:**
    - LIDAR Location: T10
    - Backsight: T2
    - LiDAR distance from peg: -0.86m





T10 T2 -0.86m

2. **Second Control Point:**
    - LIDAR Location: T2
    - Backsight: T4
    - LiDAR distance from the peg: -1.26m





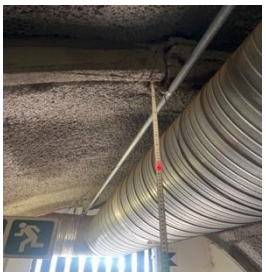
T2 T4 -1.27m

3. **Third Control Point:**
    - LIDAR Location: T4

- Backsight: T1
- LiDAR distance from the peg: -1.27m



T4



T1



-1.27m

Appendix B LiDAR Data Acquisition in the Wits Mock Mine During the Post-Deformation Stage.

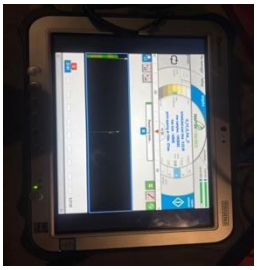
1. **First Control Point:**
    - **LiDAR Location:** T10
    - **Backsight:** T2
    - **LiDAR distance from the peg:** -0.870m



T10



T2



Controller

2. **Second Control Point:**
    - **LIDAR location:** T2
    - **Backsight:** T4
    - **LiDAR distance from the peg:** -1.305M



T2



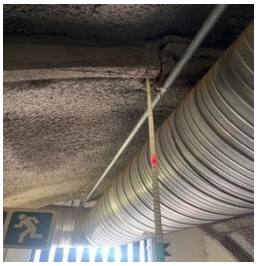
-1.305m

3. **Third Control Point**:

- LiDAR location: T4
- Backsight: T1
- LiDAR distance from the peg: -1.315m



T4



T1

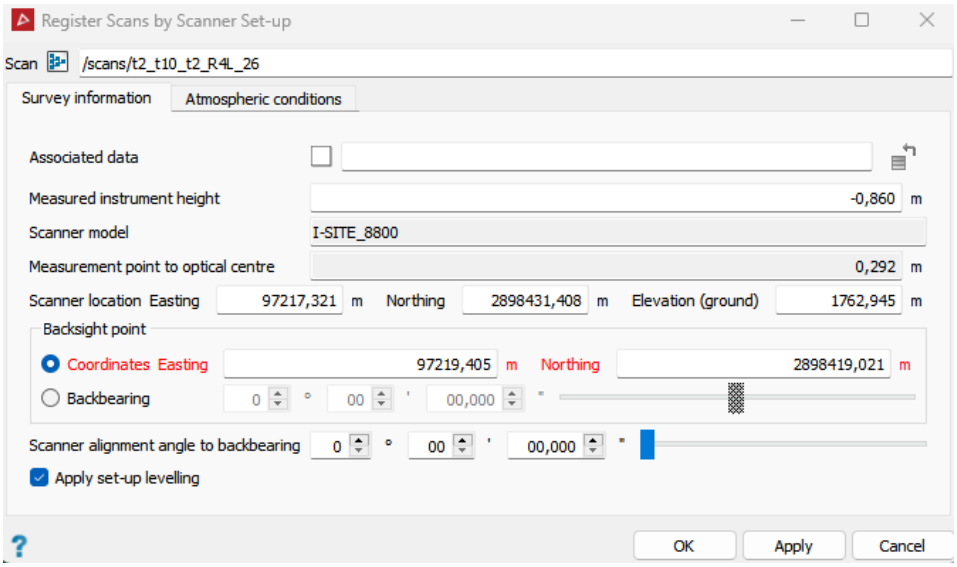


-1.315m

Appendix C Registration of Pre-Deformation and Post-Deformation LiDAR Scans.

Registration of Pre-deformation 3D model LiDAR Scans

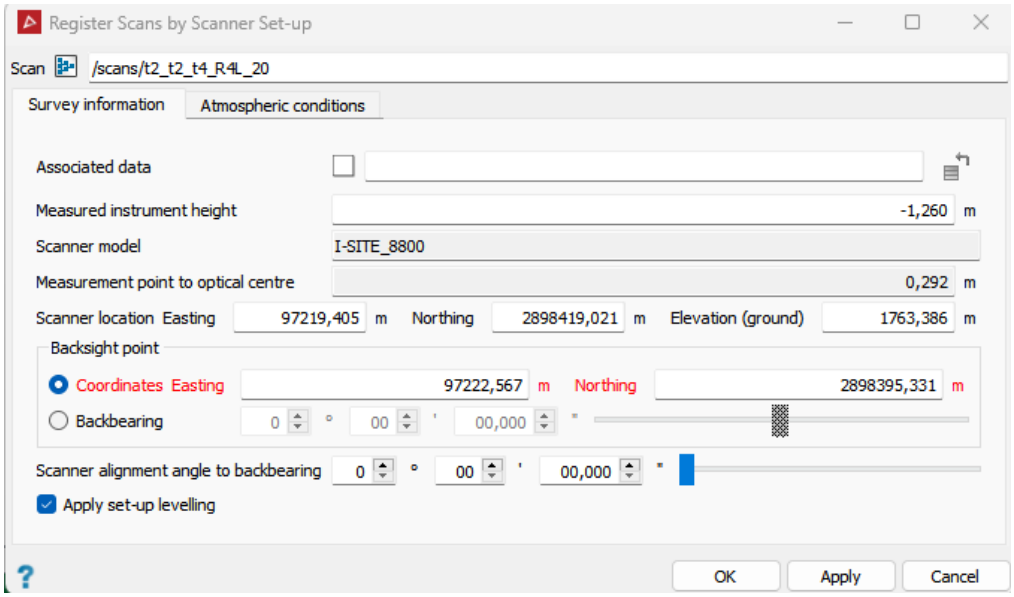
Peg T10 position



Register Scans by Scanner Set-up

Register scanner for scan /scans/t2_t10_t2_R4L_26			
Scanner location	E: 97 217,321m	N: 2 898 431,408m	RL: 1 762,945m
Measured instrument height	-0,860m		
Vector offset for I-SITE_8800 scanner	X: 0,000m	Y: 0,000m	Z: 0,292m
Backsight point	E: 97 219,405m	N: 2 898 419,021m	
Backbearing	170° 26' 26.283"		
Backsight azimuth	0° 00' 00.000"		
Backsight elevation	0° 00' 00.000"		
Scanner alignment to backbearing	0° 00' 00.000"		
Scan origin	X: 97 217,322m	Y: 2 898 431,390m	Z: 1 762,377m
Scanner bearing offset	170° 26' 26.283"		
Level correction applied	1° 46' 44.213"		

Peg T2 position

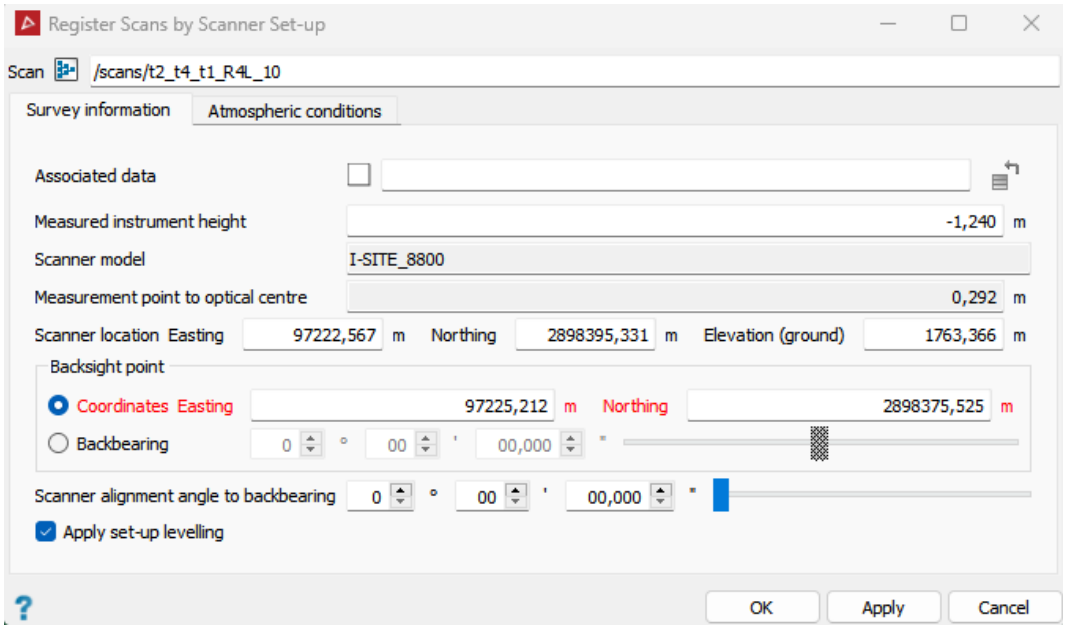


Register Scans by Scanner Set-up

Register scanner for scan /scans/t2_t2_t4_R4L_20

Scanner location	E: 97 219,405m	N: 2 898 419,021m	RL: 1 763,386m
Measured instrument height	-1,260m		
Vector offset for I-SITE_8800 scanner	X: 0,000m	Y: 0,000m	Z: 0,292m
Backsight point	E: 97 222,567m	N: 2 898 395,331m	
Backbearing	172° 28' 15.128"		
Backsight azimuth	0° 00' 00.000"		
Backsight elevation	0° 00' 00.000"		
Scanner alignment to backbearing	0° 00' 00.000"		
Scan origin	X: 97 219,441m	Y: 2 898 418,981m	Z: 1 762,419m
Scanner bearing offset	172° 28' 15.128"		
Level correction applied	3° 10' 41.798"		

Peg T4 position



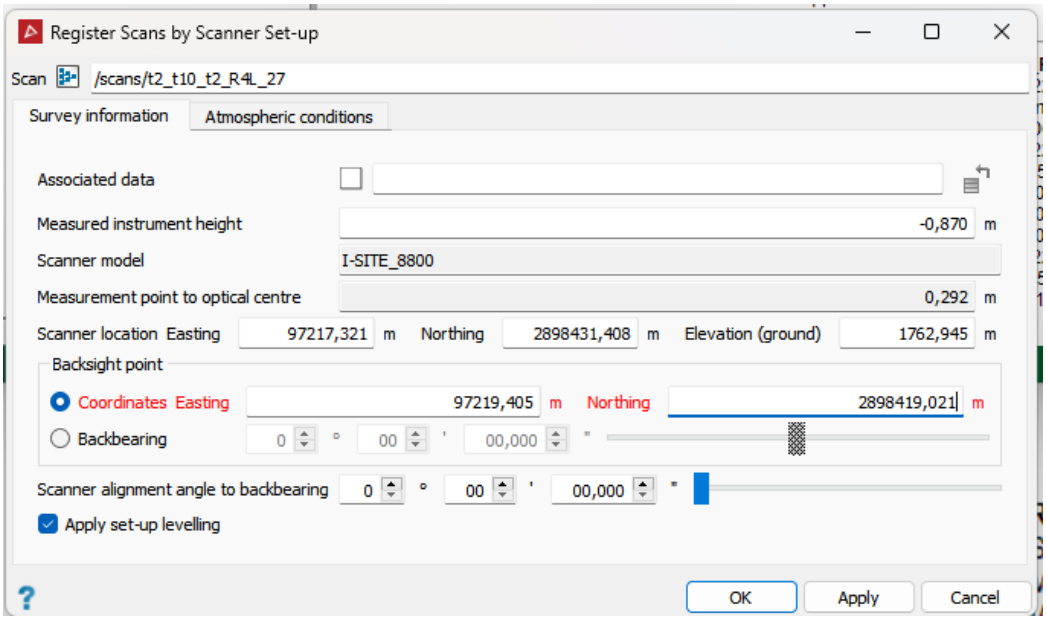
Register Scans by Scanner Set-up

Register scanner for scan /scans/t2_t4_t1_R4L_10

Scanner location	E: 97 222,567m	N: 2 898 395,331m	RL: 1 763,366m
Measured instrument height	-1,240m		
Vector offset for I-SITE_8800 scanner	X: 0,000m	Y: 0,000m	Z: 0,292m
Backsight point	E: 97 225,212m	N: 2 898 375,525m	
Backbearing	172° 25' 34.674"		
Backsight azimuth	0° 00' 00.000"		
Backsight elevation	0° 00' 00.000"		
Scanner alignment to backbearing	0° 00' 00.000"		
Scan origin	X: 97 222,577m	Y: 2 898 395,344m	Z: 1 762,418m
Scanner bearing offset	172° 25' 34.674"		
Level correction applied	0° 59' 44.243"		

Registration of post-deformation 3D Model LiDAR Scans

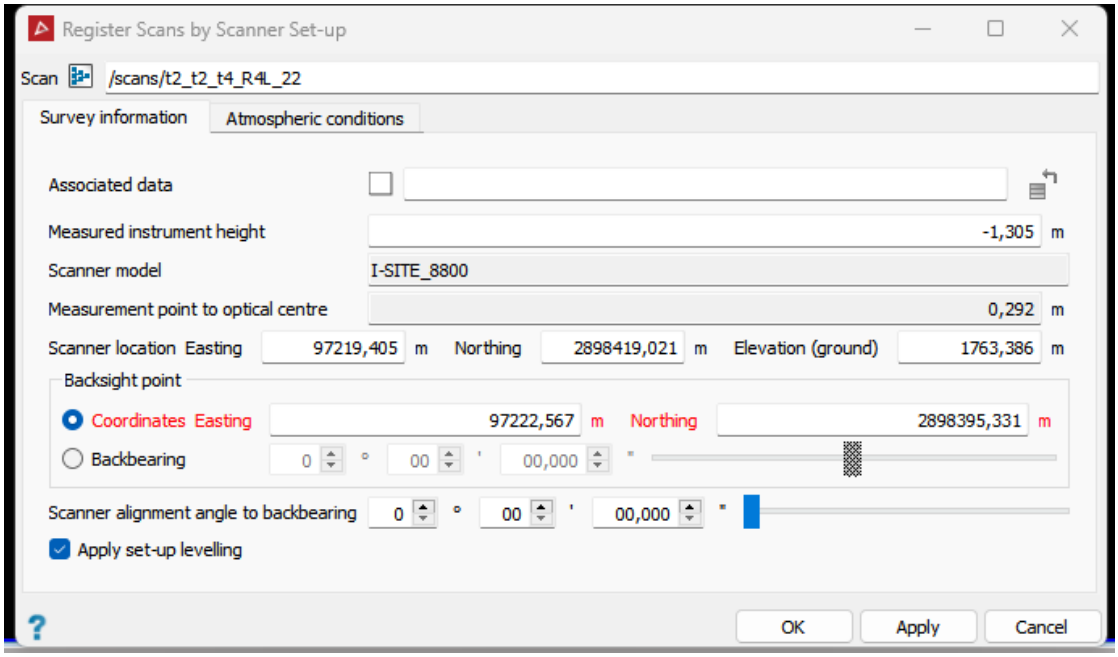
Peg T10 position



Register Scans by Scanner Set-up

Register scanner for scan /scans/t2_t10_t2_R4L_27			
Scanner location	E: 97 217,321m	N: 2 898 431,408m	RL: 1 762,945m
Measured instrument height	-0,850m		
Vector offset for I-SITE_8800 scanner	X: 0,000m	Y: 0,000m	Z: 0,292m
Backsight point	E: 97 219,405m	N: 2 898 419,021m	
Backbearing	170° 29' 44.765"		
Backsight azimuth	0° 00' 00.000"		
Backsight elevation	0° 00' 00.000"		
Scanner alignment to backbearing	0° 00' 00.000"		
Scan origin	X: 97 217,328m	Y: 2 898 431,428m	Z: 1 762,387m
Scanner bearing offset	170° 29' 44.765"		
Level correction applied	2° 08' 02.415"		

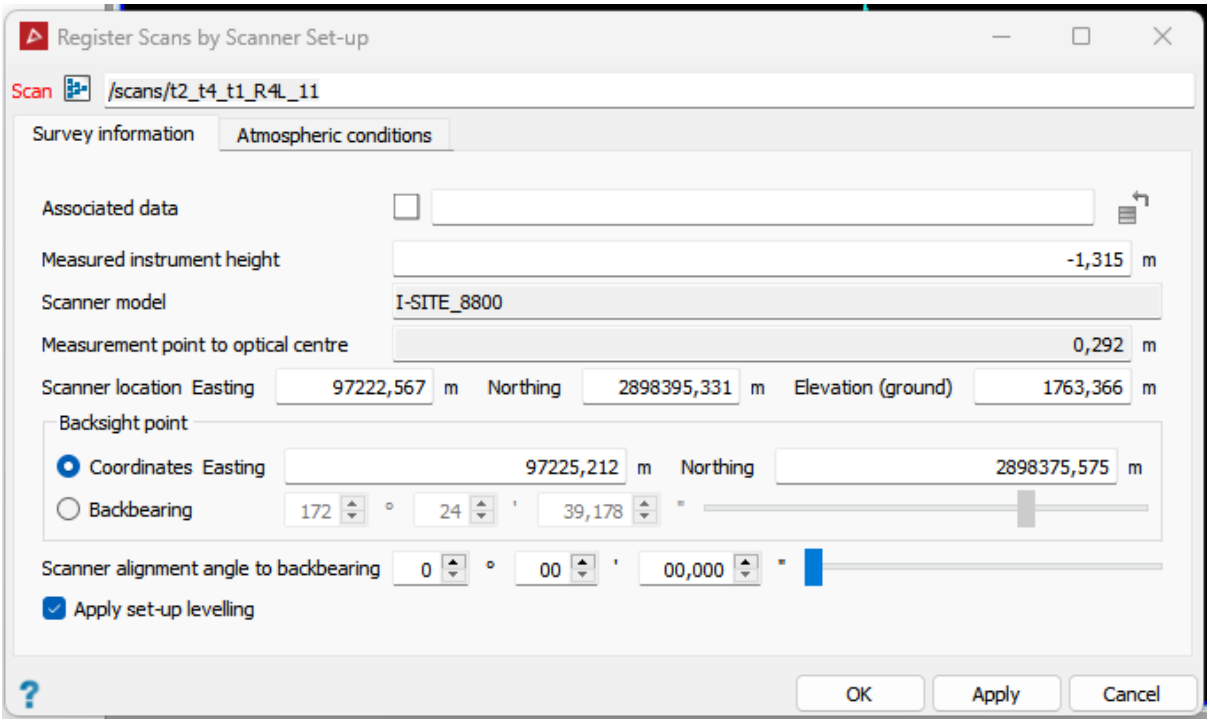
Peg T2 position



Register Scans by Scanner Set-up

Register scanner for scan /scans/t2_t2_t4_R4L_22

Scanner location	E: 97 219,405m	N: 2 898 419,021m	RL: 1 763,386m
Measured instrument height	-1,305m		
Vector offset for I-SITE_8800 scanner	X: 0,000m	Y: 0,000m	Z: 0,292m
Backsight point	E: 97 222,567m	N: 2 898 395,331m	
Backbearing	172° 19' 17.507"		
Backsight azimuth	0° 00' 00.000"		
Backsight elevation	0° 00' 00.000"		
Scanner alignment to backbearing	0° 00' 00.000"		
Scan origin	X: 97 219,375m	Y: 2 898 419,005m	Z: 1 762,374m
Scanner bearing offset	172° 19' 17.507"		
Level correction applied	1° 54' 34.394"		

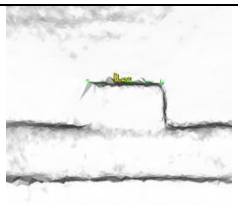
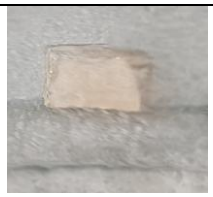
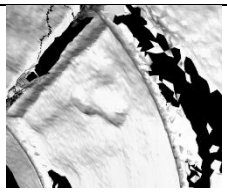
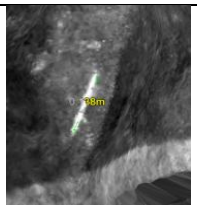


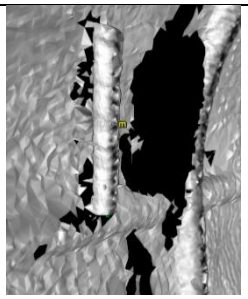
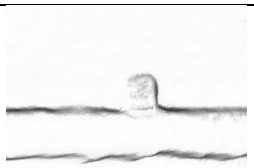
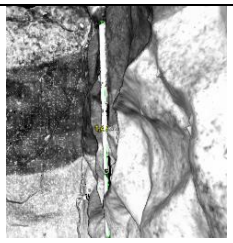
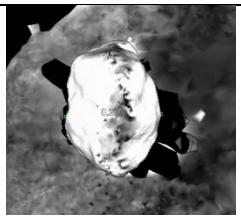
Register Scans by Scanner Set-up

Register scanner for scan /scans/t2_t4_t1_R4L_11

Scanner location	E: 97 222,567m	N: 2 898 395,331m	RL: 1 763,366m
Measured instrument height	-1,315m		
Vector offset for I-SITE_8800 scanner	X: 0,000m	Y: 0,000m	Z: 0,292m
Backsight point	E: 97 225,212m	N: 2 898 375,575m	
Backbearing	172° 24' 39.178"		
Backsight azimuth	0° 00' 00.000"		
Backsight elevation	0° 00' 00.000"		
Scanner alignment to backbearing	0° 00' 00.000"		
Scan origin	X: 97 222,585m	Y: 2 898 395,290m	Z: 1 762,344m
Scanner bearing offset	172° 24' 39.178"		
Level correction applied	2° 31' 11.959"		

Appendix D Comparison of geometry and colour of objects from CRP, LiDAR and fused 3D model.

	CRP	LiDAR	FUSED
1. Brick			
2. Plastic cup			
3. Plastic plate			
4. Pencil			

5. Cylindrical container			
6. Concrete Rock			
7. Fluorescent tube			
8. Spherical paper			

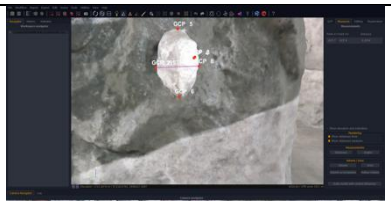
Appendix E Conventional Measurements of Objects using a Tape Measure

Object	Images	Measurements
1. Brick	Length  Width 	Length: 0.207m Width: 0.105m
2. Plastic cup		Length: 0.084m
3. Plastic plate		Diameter: 0.17m
4. Pencil		Length: 0.17m
5. Cylindrical container		Length: 0.67m

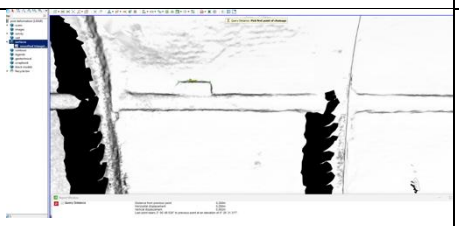
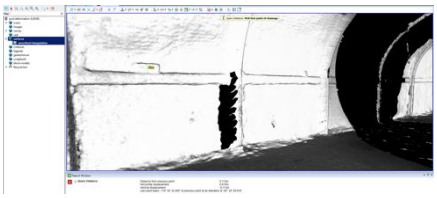
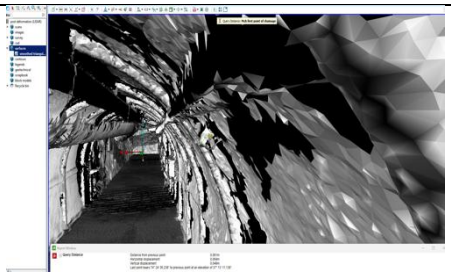
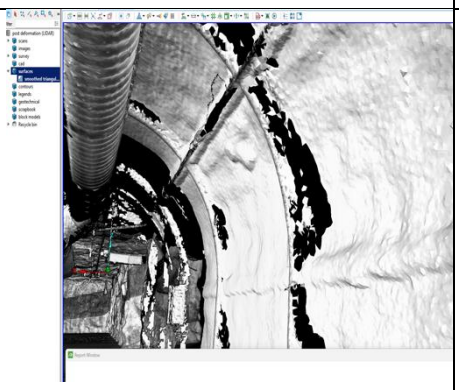
		
6. Concrete Rock	Length  Width 	Length: 0.10m Width: 0.075m
7. Fluorescent tube	 	Length: 1.50m
8. Spherical paper		Diameter: 0.35m

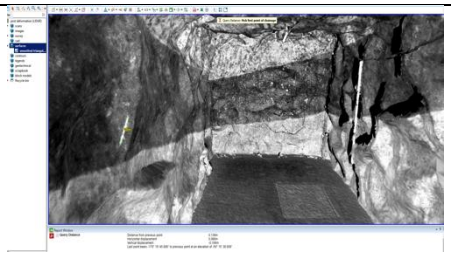
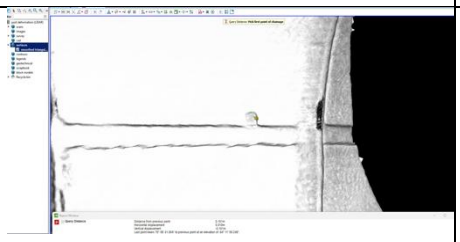
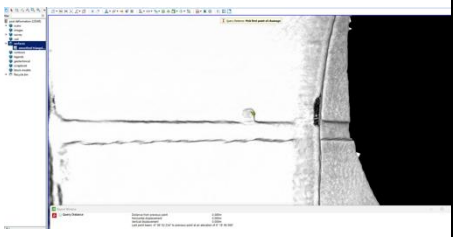
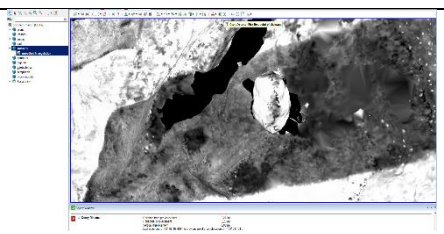
Appendix F Measurement of Objects using CRP.

Object	Images	Measurements
1. Brick	 	Length = 0.2173m Width = 0.1079m
2. Plastic cup		Length = 0.0862m
3. Plastic plate		Diameter = 0.1489m
4. Pencil		Length = 0.1509m
5. Cylindrical container		Length = 0.6764m

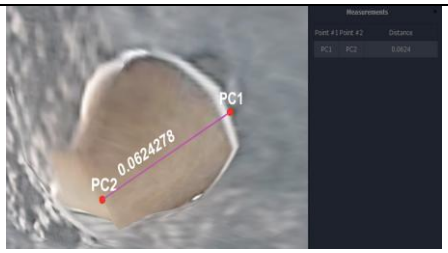
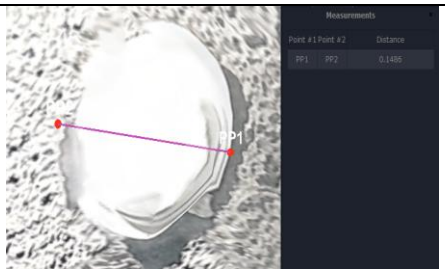
6. Concrete Rock	 	Length = 0.0880m Width = 0.0845m
7. Fluorescent tube		Length = 1.3624m
8. Spherical paper		Diameter = 0.2954m

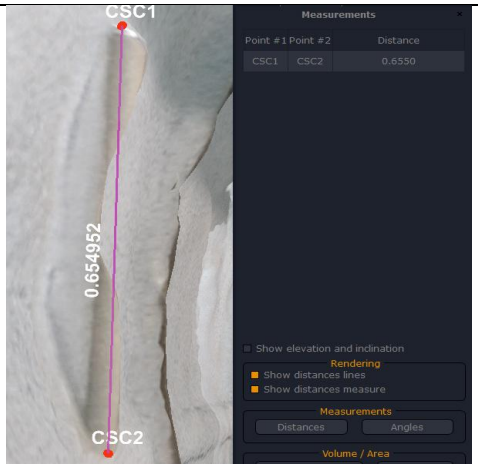
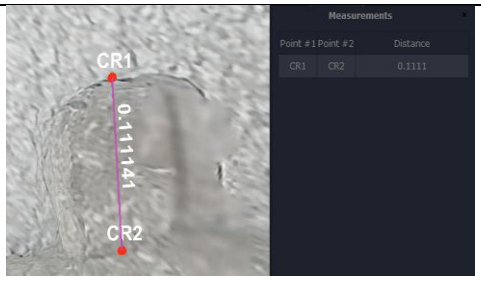
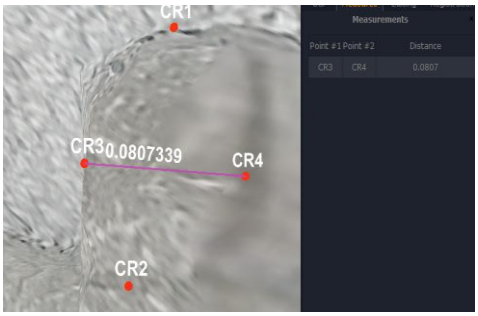
Appendix G Measurement of Objects using LiDAR.

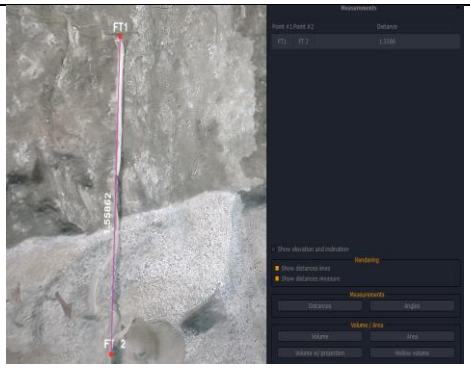
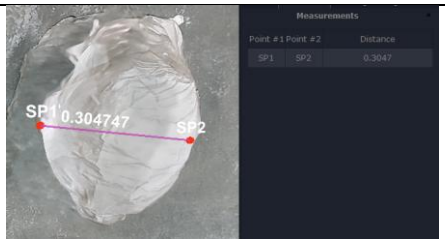
Object	Images	Measurements
1. Brick	 	Length = 0.280m Width = 0.113m
2. Plastic cup		Length = 0.081m
3. Plastic plate		Deformed

4. Pencil		Length = 0.138m
5. Cylindrical container		Length = 0.664m
6. Concrete Rock	 	Length = 0.101m Width = 0.085m
7. Fluorescent tube		Length = 1.492m
8. Spherical paper		Diameter = 0.270m

Appendix H Measurement of Objects using Fused 3D Reconstructed Model.

Object	Images	Measurements
1. Brick	 	Length = 0.2195m Width = 0.1022m
2. Plastic cup		Length = 0.0624m
3. Plastic plate		Diameter = 0.1486m

4. Pencil		Length = 0.1845m
5. Cylindrical container		Length = 0.655m
6. Concrete Rock	 	Length = 0.1111m Width = 0.0807m

7. Fluorescent tube		Length = 1.5586m
8. Spherical paper		Diameter = 0.3047m

Ethical Clearance Certificate



Zertifikat
Certificat
Certificado
Certificate

TRREE

Promouvoir les plus hauts standards éthiques dans la protection des participants à la recherche biomédicale
Promoting the highest ethical standards in the protection of biomedical research participants

Certificat de formation - Training Certificate

Ce document atteste que - this document certifies that

Clinical Trials Centre
The University of Hong Kong

Farai Musiyiwa

a complété avec succès - has successfully completed

Module 1 (2023) - Introduction to Research Ethics

du programme de formation TRREE en évaluation éthique de la recherche
of the TRREE training programme in research ethics evaluation

Release Date: 2024/01/31

Professeur Dominique Sprumont
Coordinateur TRREE Coordinator

APPROVED BY SIWF FMH ISFM

Fœderatio Pharmaceutica Helvetiae

FPH
Programmes de formation postgraduée et continue

Ce programme est soutenu par - This program is supported by :